Microseismicity of an unstable rock mass: from field monitoring to laboratory testing

C. Colombero[1*], C. Comina[1], S. Vinciguerra[1] and P. Benson[2]

[1]Dipartimento di Scienze della Terra, Università degli Studi di Torino, Italy

[2]Rock Mechanics Laboratory, School of Earth an Environmental Sciences, University of Portsmouth, UK

Corresponding author: Chiara Colombero (chiara.colombero@unito.it)

Key Points:

- The microseismicity of an unstable cliff is studied using spectral analysis, source location, event-rate correlation with external factors
- AE laboratory tests are performed to reproduce the site microseismicity under controlled fluid and temperature conditions
- Thermal stresses are found to be the main cause inducing micro-cracking processes at both the field and laboratory scale

Abstract

The field-scale microseismic (MS) activity of an unstable rock mass is known to be an important tool to assess damage and cracking processes eventually leading to macroscopic failures. However, MS-event rates alone may not be enough for a complete understanding of the trigger mechanisms of mechanical instabilities. Acoustic Emission (AE) techniques at the laboratory scale can be used to provide complementary information. In this study, we report a MS/AE comparison to assess the stability of a granitic rock mass in the northwestern Italian Alps (Madonna del Sasso). An attempt to bridge the gap between the two different scales of observation, and the different site and laboratory conditions, is undertaken to gain insights on the rock-mass behavior as a function of external governing factors. Time- and frequency-domain parameters of the MS/AE waveforms are compared and discussed with this aim. At the field scale, special attention is devoted to the correlation of the MS-event rate with meteorological parameters (air temperature and rainfalls). At the laboratory scale, AE rates, waveforms and spectral content, recorded under controlled temperature and fluid conditions, are analyzed in order to better constrain the physical mechanisms responsible for the observed field patterns. The integration of the results allowed for an interpretation of the factors potentially governing the mechanical instability at the site confirming abrupt thermal variations as the main cause of the site microseismicity, without highlighting irreversible acceleration in the MS-event rate potentially anticipating the rock mass collapse.

1 Introduction

The microseismic activity of an unstable rock mass represents a useful tool with which to assess damage and early-stage cracking processes that may eventually lead to macroscopic failures. The analysis of the fracture-related microseismic (MS) events, in terms of temporal rate and source locations, can provide useful information on the acceleration to failure and on the identification of the most prone-to-fail compartments and slip surfaces. However, MS events alone may not be enough for a complete understanding of the factors governing mechanical instabilities, particularly in complex field environments where it is difficult to directly link external stimuli to environmental considerations. To better understand these stimuli, field analyses are often complemented with acoustic emission (AE) experiments at the laboratory scale. Laboratory tests have the advantage of controlled boundary conditions (e.g. water content and temperature) in a controlled and systematic manner. Since the early 1970s, there has been an increasing interest in the use of AE/MS techniques for field and laboratory investigations of geological materials and engineering applications. These studies apply to different scales and investigation environments, using a different frequency range of the microseismic activity [*Hardy*, 2003], varying from 1-100 Hz (MS) to the kHz-to-MHz range (AE).

In the last 20 years, MS recording has been extensively deployed on a variety of rock-mass settings, ranging from pre-eruptive volcanic edifices and lahars [e.g. *Diodati et al.*, 1991; *Gambino et al.*, 2004] to debris flows and ice avalanches [e.g. *Caplan-Auerbach and Huggel*, 2007] and mining environments [e.g. *Young and Collins*, 2001]. Dealing with rock-slope stability, *Amitrano et al.* [2005] and *Senfaute et al.* [2009], examined the microseismic signals recorded prior to the collapse of a 2000-m^3 coastal cliff sector located at Mesnil-Val (Normandie, France), demonstrating that MS events can provide information about the incipient failure of internal rock bridges. After this study, applications of the method expanded to several test sites, especially in the Alpine context. These monitoring locations led to large datasets of

recorded events [e.g. in *Spillman et al.*, 2007; *Walter and Joswig*, 2009; *Amitrano et al.*, 2010; *Helmstetter and Garambois*, 2010 and *Lévy et al.*, 2011], with challenging classification and location tasks due to the strong heterogeneities in the seismic velocity field characterizing the unstable slopes, which gives rise to strong signal scattering and attenuation. Consequently, a large part of these studies were mainly focused on the search for seismic precursors before slope failure and on the relation between seismic events (ruptures, rockfalls), displacement rate measurements, and external governing factors (particularly climatic parameters).

Numerous external factors can promote slope instabilities. The most widespread factors include excessive rainfall and the consequent modification of the hydrogeological parameters of the unstable bodies, freeze-thaw cycles and snow melting, temperature variations, earthquake shaking, volcanic activity, and human action [*Gariano and Guzzetti*, 2016]. Although these triggering causes are globally accepted, their influence on possible instabilities are strongly dependent on the nature of the unstable body and on the site location (elevation, exposure and climate). Depending on the environmental factors, the influence of one or some of these key triggers may therefore dominate on the other external parameters. For example, rockslides and rockfalls located in high mountainous areas (hard rocks and freezing climate) are mostly driven by temperature variations [*Paranunzio et al.,* 2015]. However, although individual mechanisms of physical weathering have been addressed through field studies [e.g. *McFadden et al.*, 2005; *Eppes et al.*, 2010], numerical modeling [e.g. *Moores et al.*, 2008], and laboratory experiments [e.g. *McKay et al.*, 2009; *Molaro and McKay*, 2010], few study have been able to demonstrate an unequivocal correlation between environmental factors and rock cracking. Besides rapid thermal shocks, there are a large number of cyclic processes acting on rock masses, which constitute physical weathering agents [*McFadden et al.*, 2005; *McKay*, 2009; *Moores*, 2008; *Eppes et al.*, 2010]. These include daily and seasonal cycles and other short-term heating-cooling cycles (effect of wind), wetting-drying cycles, and freeze-thaw cycles. *Gunzburger et al.* [2005] demonstrated that daily thermal cycles are able to induce shearing along existing fractures, particularly when temporal or spatial temperature gradients are the highest. Since an increase in moisture reduces the tensile strength and fatigue limit of the rock [*Burdine et al.*, 1963], the combined effect of moisture and temperature is likely to enhance thermal expansion and contraction processes [*Yatsu*, 1988; *Halsey*, 1996]. Given these preconditions, and since microseismicity has proven to be a valuable tool to infer incipient fracture processes, correlations between meteorological factors and the MS event rate have often been attempted. In particular, the Séchilienne landslide (French Alps) exhibited clusters of microseismicity that were weakly but nonetheless correlated with rainfall [*Helmstetter and Garambois*, 2010]. Although rockfalls occurred on a regular basis with respect to the instance of precipitation, a strong variation in the numbers of rockfalls per day was noted even for the same rainfall intensity, making a trigger threshold impossible to establish. From the combined analysis of rainfall and temperature data, *Lévy et al.* [2010] found that an increase in the microseismicity of an unstable rock column could be correlated with probable freeze-thaw cycles. Due to the environmental conditions common to the Matterhorn Peak (3829 m a.s.l.), *Amitrano et al.* [2010] used air temperature to investigate possible relations between seasonal temperature variation and slope deformation. Here, clusters of MS events occurred in specific days characterized by abrupt negative or positive temperature changes. *Amitrano et al.* [2012] and *Girard et al.* [2013] further demonstrated thermal and freezing-induced stresses as crucial micro-fracturing causes in high-altitude rock faces, by means of on-site AE monitoring.

Conversely, *Spillman et al.* [2007] did not find either obvious seasonal variations or correlations between temperature/rainfalls and microseismicity recorded at the Randa gneissic rockslide (Swiss Alps). Importantly, in all of these studies, air temperature and rainfall trends are the only external parameters which have been tentatively correlated to the microseismic activity in unstable sites, albeit inconsistently.

Due to these inconsistencies, partially related to the variability of natural environments, new experiments at an intermediate scale between field and laboratory were conducted in an attempt to link these factors to weathering [*Garbini*, 2009; *Swami*, 2011 and *Warren et al.*, 2013]. Here, long-term multi-sensor studies of acoustic emissions on small-size granitic boulders exposed to ambient conditions were conducted. The surface of each natural block was instrumented with AE sensors, strain gauges, thermocouples and a surface moisture sensor. During a six-month monitoring campaign, AE events were typically observed to cluster during late afternoon and evening hours, and related to sudden drops or rises of surface temperature. These negative/positive thermal shocks were directly correlated to surface strain variations, indicating contraction/expansion of the boulder. While the highest number of AE events occurred when the rock was wet, a significant number of events was still detected in dry conditions. Even when AE events occurred during precipitations, dry AE events often preceded the rainfall occurrence.

In this study, we present a microseismicity study of an unstable granitic cliff located in northwestern Italian Alps (Madonna del Sasso, VB), combined with laboratory rock-physics experiments to better understand the gap in observation scale. At the field scale, particular attention is devoted to search for correlations between the long-term MS-event rate and the meteorological parameters (rainfall and temperature). On this basis, appropriate AE emission laboratory tests have been developed for qualitative comparison. This makes use of both AE rate and spectral content as a function of controlled temperature and fluid conditions, so as to better constrain the physical mechanisms responsible for the observed field patterns. Such laboratory tests, integrating conventional triaxial apparatus with AE recordings, have already been proven to give experimental insights to fracture nucleation, growth and coalescence into major fractures and in the underlying micromechanisms [*Lockner et al.*, 1991]. These studies always referred to investigation targets located at considerable depths, varying from tunneling applications to volcanic systems and earthquake dynamics ; *Browning et al.*, 2016 The adopted laboratory instrumentations and loading conditions were therefore justified by the site stress fields. Semi-quantitative AE/MS comparisons could consequently be established considering similarities between laboratory and field waveforms (e.g. amplitude and duration) or related spectral contents (i.e. similarities in the spectrograms), in order to characterize the mechanism controlling the frequencies distribution [e.g. *Burlini et al.*, 2007; *Benson et al.*, 2008; *Benson et al.*, 2010; *Fazio et al.*, 2017]. However, the present study has different near-surface site conditions imposed by an outcropping fractured cliff. Here, loading conditions are essentially controlled by gravity, with superimposed stress and strain fluctuations driven by external factors or internal fluid pressure. The adopted laboratory procedure was thus chosen as a compromise between the available testing instrumentation and the need of studying the influence of temperature and fluids on fractured samples, in order to have a proxy for the factors controlling the microseismicity of the site. The triaxial apparatus was first used to obtain fractures within the samples. After failure, axial load was reduced to the 75% of the residual value and differential stress was set to remain constant, in order to allow the sample to expand and contract in both axial and radial direction. This approximately simulates “free conditions” in the samples, ensuring at all times not to

exceed a deformation threshold leading to slip along the fault plane. In this configuration, samples were then heated and cooled both in dry and wet conditions, to analyze the AE waveforms related to thermal cracking and fluid flow within the fractures.

2 Microseismicity at the field scale

2.1 Test site and monitoring network

In October 2013, a microseismic monitoring network was installed in the surroundings of the XIII-century church of Madonna del Sasso, in northwestern Italian Alps (Fig. 1a). The site is located on the western shore of the Orta Lake, at the top of a steep homogeneous granitic cliff (*Granito di Alzo*), delimited by sub-vertical faces on the north, south and east sides (Fig. 1b). The cliff lies close to the NE edge of the SW-NE elongated Alzo-Roccapietra Pluton, which is delimited by three main faults: the Pogallo Line, to the west, the Cossato-Mergozzo-Brissago Line, to the east, and the Cremosina Line, to the south [*Boriani et al.,* 1990; *Boriani and Giobbi*, 2004].

Near the summit of the cliff, two potentially unstable blocks are partially isolated from the stable rock mass by the presence of four main deep and open fractures (K1 to K4, in Fig. 1c and Fig. 1d). In particular, the first block "A" is limited on the vertical sides by fractures K2, K1 and K4 at the northern edge of the cliff. The second southern block "B" is cut by fractures K2 and K4. Both A and B are truncated at the base by K3 (Fig. 1c and Fig. 1d). Fracture orientations partially reflect the orientations of the main tectonic lineaments of the area. Regional stresses could have therefore contributed to fracture formation, but since no recent tectonic activity is highlighted on these regional faults, the present fracture configuration is expected to be mainly driven by gravity and external weathering factors.

Displacements, localized collapses in the yard at the top of the cliff and progressive fracture opening with associated intense air upflows, have been observed and measured on site, since 1981. Given the almost inaccessible steep morphology of the cliff, a complete characterization of the 3-D fracture setting was achieved from the combination of field observations, non-contact measurements of fracture orientations on a 3-D georeferenced model of the cliff (obtained from a laser-scanning and photogrammetric survey), active and passive seismic surveys [*Colombero et al.*, 2016; *Colombero et al.*, 2017]. These results highlighted a predominant control of fractures K4 and K2 on the stability of the site. These fractures have indeed the largest opening (~0.5 m) and persistence within the rock mass [~15 m, from *Colombero et al.,* 2017]. Past displacement monitoring campaigns at the site (crackmeters on fractures K1 and K2 in 1991-1992 and wire extensometers across fracture K4 in 2008-2009) highlighted a partially reversible seasonal fluctuation of fracture opening, driven by air temperature fluctuations [*Regione Piemonte*, 1993]. In particular, maximum fracture opening was recorded during winter months, likely due to the rock-mass thermal contraction, while minimum opening was found in summer as a result of the rock-mass thermal expansion. In addition, the maximum opening values were recorded at the top of the cliff (3 mm/yr, with residual displacement of approximately 2 mm/yr) while measurements at lower altitudes across the same fractures showed lower displacement rates (1.3 mm/yr, with no residual displacement), suggesting a foot control on the block displacements [*Colombero et al.*, 2016]. From topographic measurements (carried out twice/year at the top block A by ARPA Piemonte, since 2006),

comparable accumulating residual displacements of approximately 2 mm/yr in ENE direction (perpendicularly to fracture K4) and -2.7 mm/yr along the vertical plane are measured.

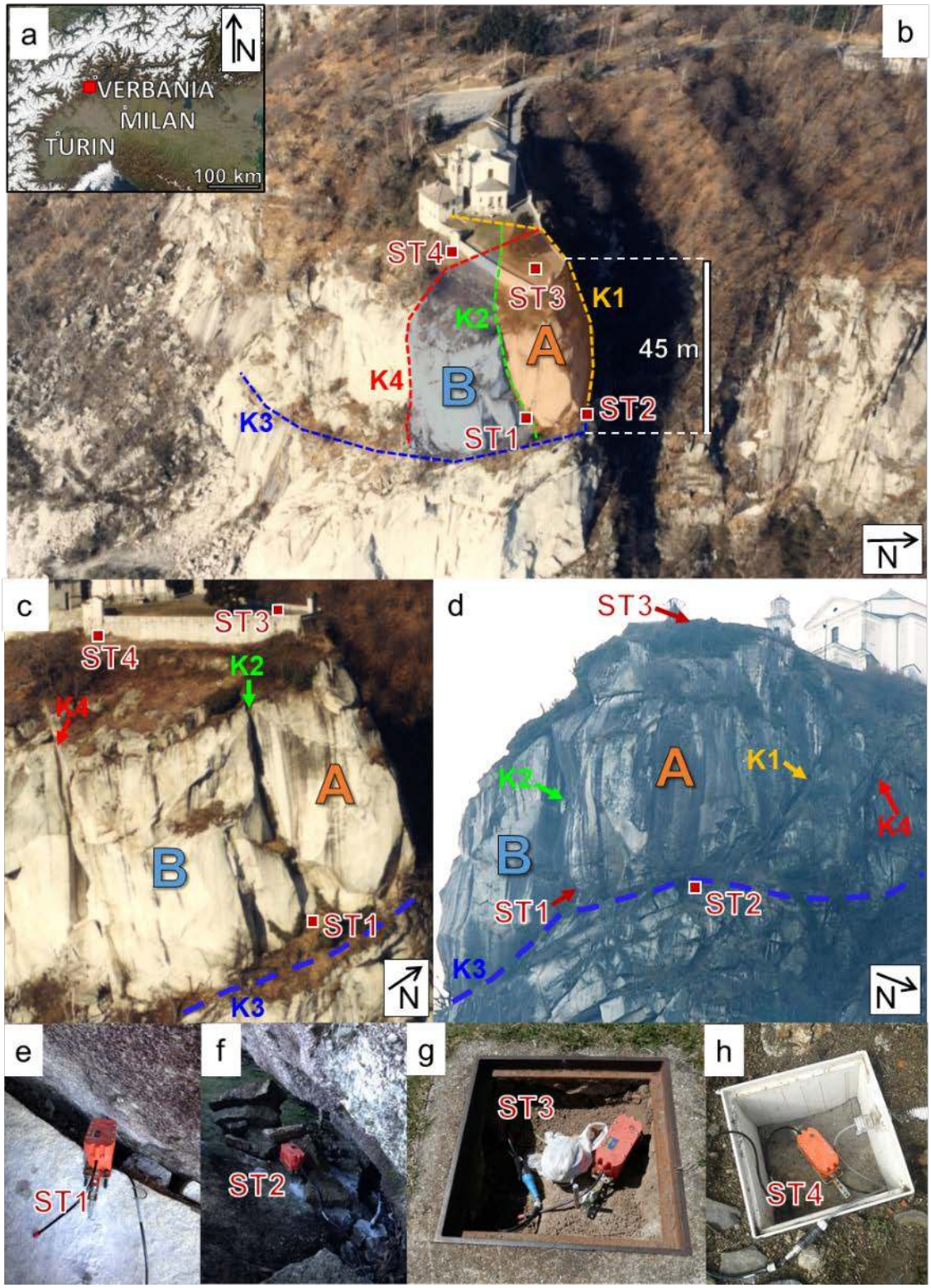

Figure 1 (a) Geographical location of the test site (Madonna del Sasso), in northwestern Italian Alps. (b) Eastern, (c) Southern and (d) Northern aerial views of the site with indication of fracture traces (K1 to K4) and location of the microseismic stations (ST1 to ST4). The two unstable blocks are highlighted by

letters A and B. (e-h) Detail on the microseismic monitoring stations: (e) ST1, (f) ST2, (g) ST3 and (h) ST4.

The microseismic network was designed to specifically monitor the unstable block A, with four seismic stations (4.5-Hz triaxial geophones). Two stations were located near the foot of the unstable block, on the southeast (ST1, Fig. 1e) and north (ST2, Fig. 1f) faces of the cliff, while other two stations were located in shallow manholes at the cliff summit, respectively at the top of block A (ST3, Fig. 1g) and outside the fractured sector (ST4, Fig. 1h). The latter was consequently used as a reference station. Each station was fixed on a steel support (Fig. 1, e to h) and anchored approximately 5 cm deep in the granitic bedrock (ST1 and ST2) or in the basal concrete slab of the shallow manholes (for ST3 and ST4). The four stations were connected to an acquisition system (12-channel "Granite", Kinemetrics Inc.) located a few meters to the east of ST4. The system was completed by a GPS antenna, for timing and synchronization of the acquired seismic traces. Power supply was provided by direct connection to the electrical line of the site. Wireless data transmission was set to enable remote system control and data download. Short-duration seismic events were recorded at 1-kHz sampling frequency, using a STA/LTA (Short Time Average over Long Time Average) detection algorithm (STA window=0.3 s, LTA window=30 s, STA/LTA trigger threshold=6). The total number of hits (the number of times in which a channel exceeds the STA/LTA threshold) to trigger the system was set to 12, excluding contributions coming from the upper stations (ST3 and ST4), in order to reduce the recording of anthropic disturbances linked to human presence and activities on the site. Due to a breakdown of the acquisition system between August 2014 and May 2015, MS events were recorded in two main time windows: the first between October 2013 and August 2014, the second between May 2015 and February 2016. In the monitored time windows, more than 12600 seismic events were recorded, including MS events likely to be related to fracture processes within the rock mass, as well as local and regional earthquakes, electronic noise, and anthropic disturbances.

2.2 MS processing methods

Classification of the recorded dataset was performed integrating both visual analysis of the event spectrograms [*Helmstetter and Garambois*, 2010] and cluster analysis of reference parameters for each event class, including signal maximum amplitude, frequency peak in the Fourier spectrum, kurtosis and duration.

The location of the extracted MS events was then carried out using the non-linear probabilistic approach of *Lomax et al.* [2000]. To improve location results, a 3-D velocity model of the cliff was on-purpose built, combining a laser-scanning Digital Terrain Model (DTM) with the results of seismic surveying at the site [from *Colombero et al.*, 2016]. The final 3-D model has velocities varying from 300 m/s (in air, outside the rock mass) to 3200 m/s (in deep intact granite). This model was calibrated and tested by re-location of georeferenced hammer strokes performed at the cliff summit. Gaussian distribution functions were used in the non-linear probabilistic approach to represent 4-ms uncertainty in the reading of first arrival times (up to 10 m of spatial uncertainty considering the average velocity of the 3-D model= 2400 m/s) and 0.5-ms uncertainty in the theoretical travel times (corresponding to 1.2 m of uncertainty considering the 3-D model average velocity). For each located MS event, the maximum likelihood point of the complete non-linear location Probability Density Function (PDF) was finally selected as the optimal hypocenter. Due to the non-linearity of the problem, the PDFs completely describing the location results are not ellipsoidal and in some cases are somewhat irregular. Nevertheless,

traditional Gaussian estimators and related confidence ellipsoids are still useful indicators of uncertainties in the location, especially when the complete non-linear PDFs are more regular and less scattered. As a consequence, confidence ellipsoids were retrieved as well in addition to the maximum likelihood solutions, to evaluate the uncertainties in the location results.

Since spectral features and location results confirmed the fracturing-related nature of the MS signals, particular attention was finally devoted to investigate the temporal correlations and effects of temperature fluctuations and rainfalls on the MS event rate.

2.3 MS dataset: spectrograms and source location

From the original dataset, 1773 impulsive and short-duration signals possessing a triangular envelope and clear coda (Fig. 2) were recognized as possible MS events originating from micro-cracking processes. This hypothesis is supported by spectral data, that show a recurrent clear high-frequency emergent onset followed by a sudden exponential decay of the high-frequency content with time, in approximately the 75% of the event dataset (Fig. 2a and b). In the remaining 25% of the events, the high-frequency content (> 30 Hz) is partially or totally missing (Fig. 2c and d). MS events were seen to occur either as single events or in sequences of more events at different time spacing (Fig. 2e and f). All MS events showed variable amplitude, high kurtosis values and frequency peaks usually centered around 20 Hz.

The time- and frequency-domain peculiarities of the detected MS events are in agreement with those reported by several authors for MS events recorded on other unstable sites [e.g. *Helmstetter and Garambois*, 2010 and *Lévy et al.*, 2010]. At the laboratory scale, similar spectral shapes have been identified in relation to rock-sample fracturing or slip processes on pre-existing surfaces (e.g. *Burlini et al.*, 2007; *Benson et al.*, 2008 and *Benson et al.*, 2010).

The majority of MS events was recorded only by ST1 and/or ST2, which suggests low-energy events occurring close to the foot of the unstable volume. Frequently, all the three stations located on block A (ST1, ST2 and ST3) were triggered, probably indicating MS sources located within the unstable volume but unable to reach the station (ST4) located outside the fractured zone.

The location of the MS events was therefore carried out on a limited good-quality sub-dataset of 451 MS events recorded at all the four stations. Location results are reported in Figure 3. Given the high number of events in a small volume, 68% confidence ellipsoids are shown instead of the complete 3-D PDF scatter clouds (Fig. 3a). Ellipsoid semi-axial lengths vary from 3 to more than 20 m, reflecting uncertainties in the location procedure. However, the related ellipsoids are well contained within the rock mass confirming the origin of the events within the unstable compartments.

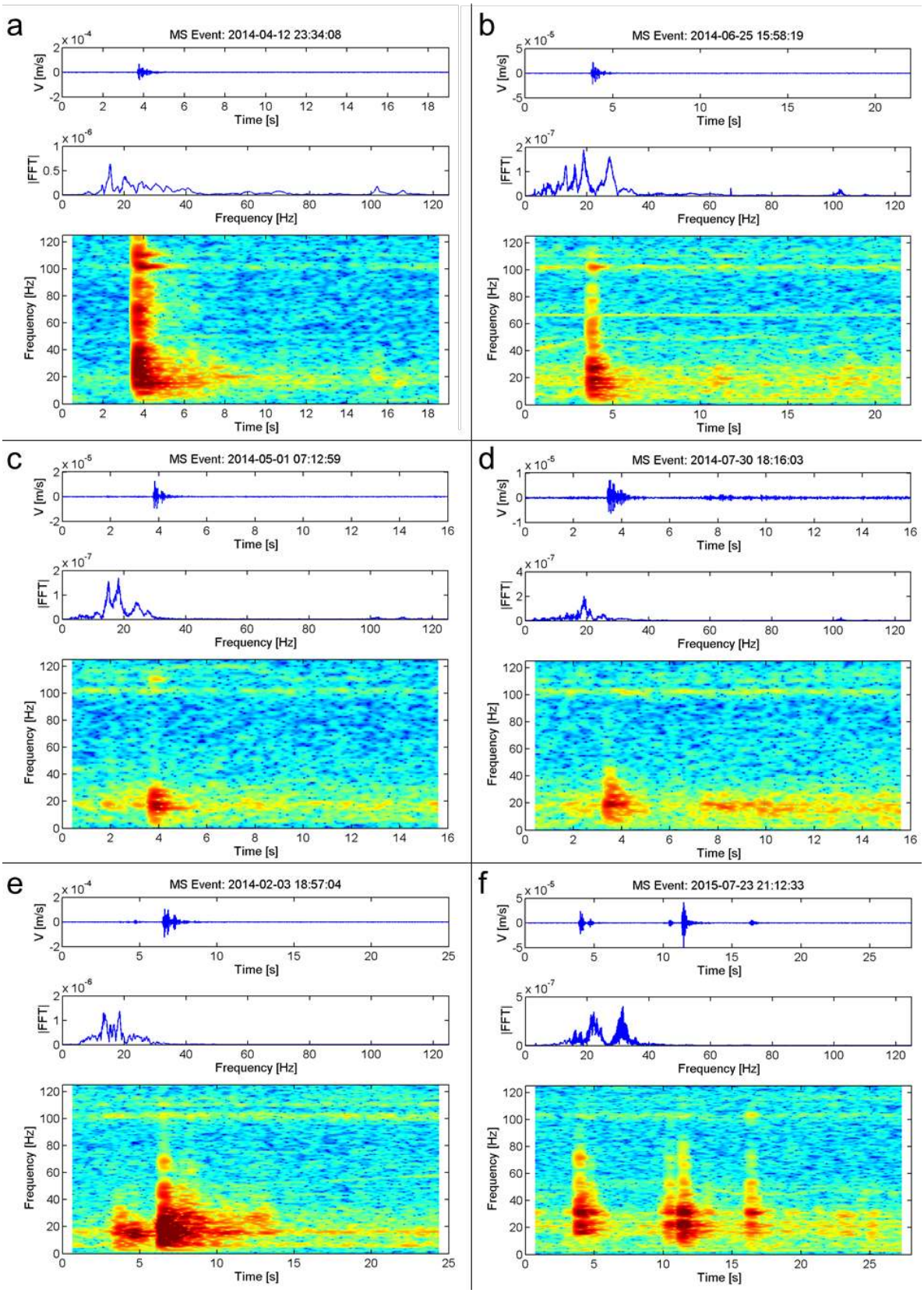

Figure 2 Examples of microseismic events recorded at Madonna del Sasso. In each section (a-f), from the top to the bottom: seismogram recorded on channel N of ST2, related Fourier spectrum and spectrogram.

Hypocenters related to the maximum likelihood solutions (Fig. 3b) mainly locate the sources of MS activity along fracture K2, with a higher concentration in the first 10 m depth, particularly between the K2 and K4 intersection. Occasional deeper MS events are also observed around the basal fracture K3.

These results seem to confirm the past direct measurements of displacement at the site and the fracture characterization based on active and passive seismic surveys. Particularly, crackmeters and extensometers recording on site during 1991-1992 and 2007-2008, already highlighted a seasonal trend of opening and closing of both fractures K2 and K4, driven by air temperature fluctuations inducing rock-mass thermal contraction and expansion [*Regione Piemonte*, 1993]. Displacements were found to be predominant at the top of the cliff, suggesting a foot control on the block stability. *Colombero et al.* [2017] detected the same temperature-driven daily and seasonal reversible variations in the resonance frequencies of the unstable compartments measured from ambient seismic noise recordings. In addition, it was demonstrated from noise spatial directivity and numerical modeling that the cliff vibration directions are mainly controlled by fracture K2 and K4, which are indeed the most persistent open fractures at the site.

MS-event locations are indeed focused in shallower parts of these two fractures. The MS-daily event rate (Fig. 3c) seems to be affected by similar seasonal fluctuations, with a maximum activity during summer months (July-August, up to 30 MS events/day) when the rock mass is expected to undergo thermal expansion and progressive fracture closing, and minimum activity in cold months (January-February, approximately 2 events/day), when rock-mass thermal contraction and fracture opening take place. These observations led to further investigate the possible influence of external factors on the MS-event rate recorded on site.

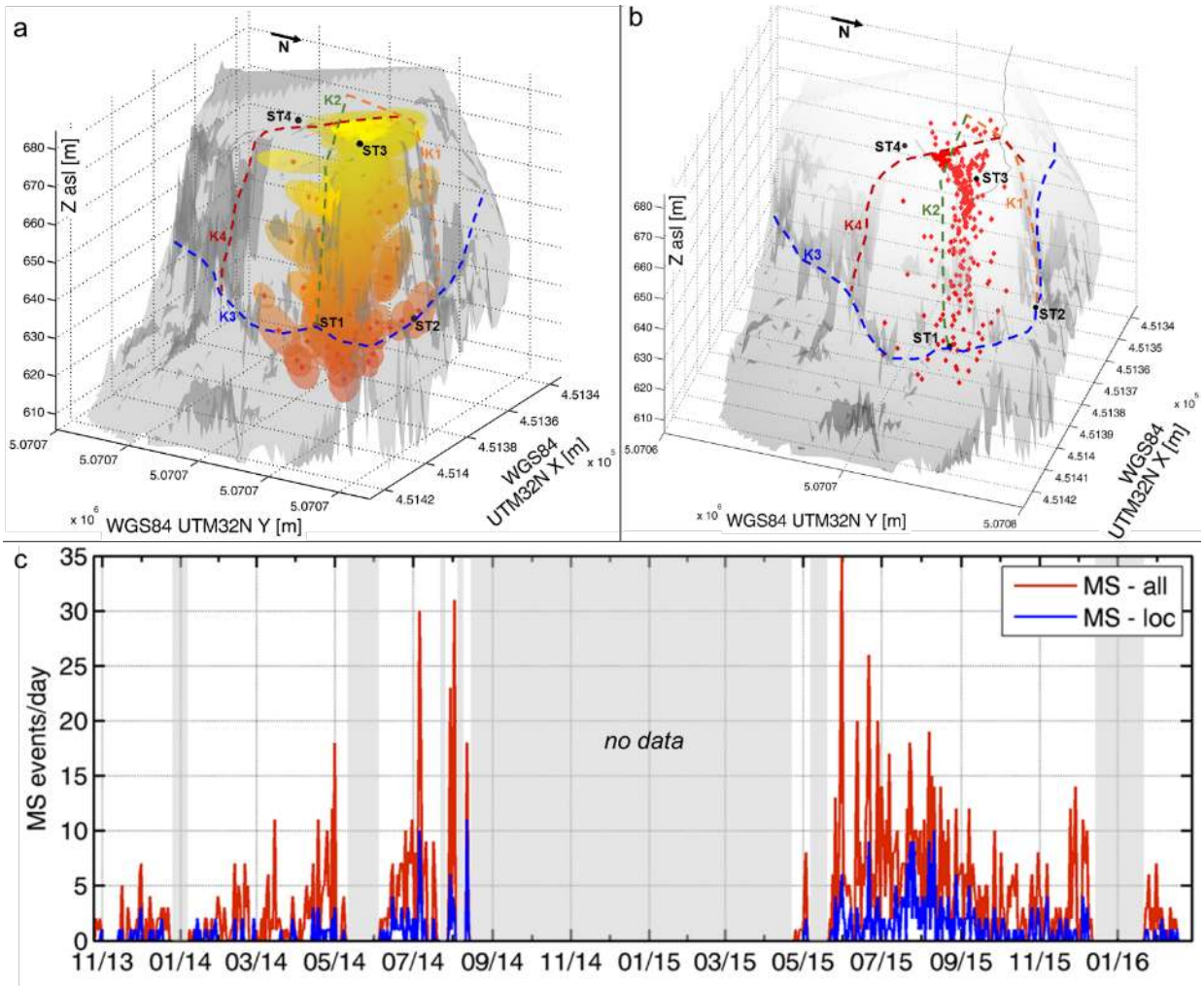

Figure 3 MS-event location. (a) 68% confidence ellipsoids referred to the location of 451 MS events. Ellipsoids are plotted in color scale from yellow to red (from surficial to deep events). The center of each ellipsoid is the Gaussian Expectation E(x), marked with the red asterisk. (b) 3-D view of the maximum likelihood solutions (optimum hypocentral location, plotted with red diamonds) for the same events. (c) Daily number of total (in red) and located (in blue) MS events.

2.4 MS dataset: correlation with external factors

Air temperature measurements were available on site for the period between January and April 2014. Temperature probes were located on the south and north faces of the cliff, and in the open fracture K2 at a depth of 10 m. Unfortunately, these three sensors were damaged few months after their installation. On-site temperature data are therefore available only for cold months, in which the number of recorded events is significantly lower than in warm months (Fig. 3c). Temperature data over the whole period (November 2013 to February 2016), are thus referred to the meteorological monitoring station of ARPA Piemonte, located in Cesara (6 km north of the site, at a comparable altitude and on the same shore of the lake). Rainfall amounts have been also considered from the same meteorological station.

Temperature data from the on-site probes are reported in Figure 4a, in comparison with the data from the meteorological station of Cesara. A similar short- and long-term trend between

the north face and the reference station is found, thus partially allowing further comparison in the periods without on-site data. Over the considered period, the south face of the cliff exhibited the highest air temperature fluctuations, with up to 20°C of variation in the same day (Fig. 4a). The average trend for the north-face temperature is similar to the south until mid February. After this date, the two temperature curves start to diverge. Also inner temperature measurements in fracture K2 are partially influenced by external fluctuations of the air temperature. Daily and seasonal temperature variations similar to the external probes, even if reduced, are observed (Fig. 4a). This confirms the significant opening and intense air circulation in fractures detected on site.

Over this period, the highest daily peak of MS-event occurrence (15/03/2014 - 11 events, Fig. 4d) is observed in correspondence to the first rapid increase in both the external and internal measurements (Fig. 4a). As shown in Figure 4b, this day is also located on a sudden temperature rise, from the highest negative temperature difference between south and north faces (-8°C) to a significant positive difference (+18°C). All the other major daily peaks ($\geq$ 5 events) are associated to rapid thermal changes, particularly as they concentrate during or immediately after periods in which the thermal difference between the south and north faces rapidly switches from negative to positive values, or shows sudden modifications due to the different insolation of the two sides of the cliff. The difference between air temperature (average of north and south face) and the deep temperature inside fracture K2, besides showing an increase from mid March, is generally more stable than the one related to the north and south faces (Fig. 4b). Daily MS-event peaks are recorded when inner temperature are both higher or lower than external temperatures.

The increase in MS activity seems therefore to be mainly driven by sudden thermal variations in temperature on the sides of the cliff. None of these MS activity peaks have associated significant rainfall amounts (Fig. 4c). The only exception is the 30/01/2014 peak (5 events), occurred in concomitance with precipitations and temperature below 0°C which could have caused local ice formation in the pre-existing fractures. The most relevant rain event in the period (23/03/2014) has no relevant MS activity associated.

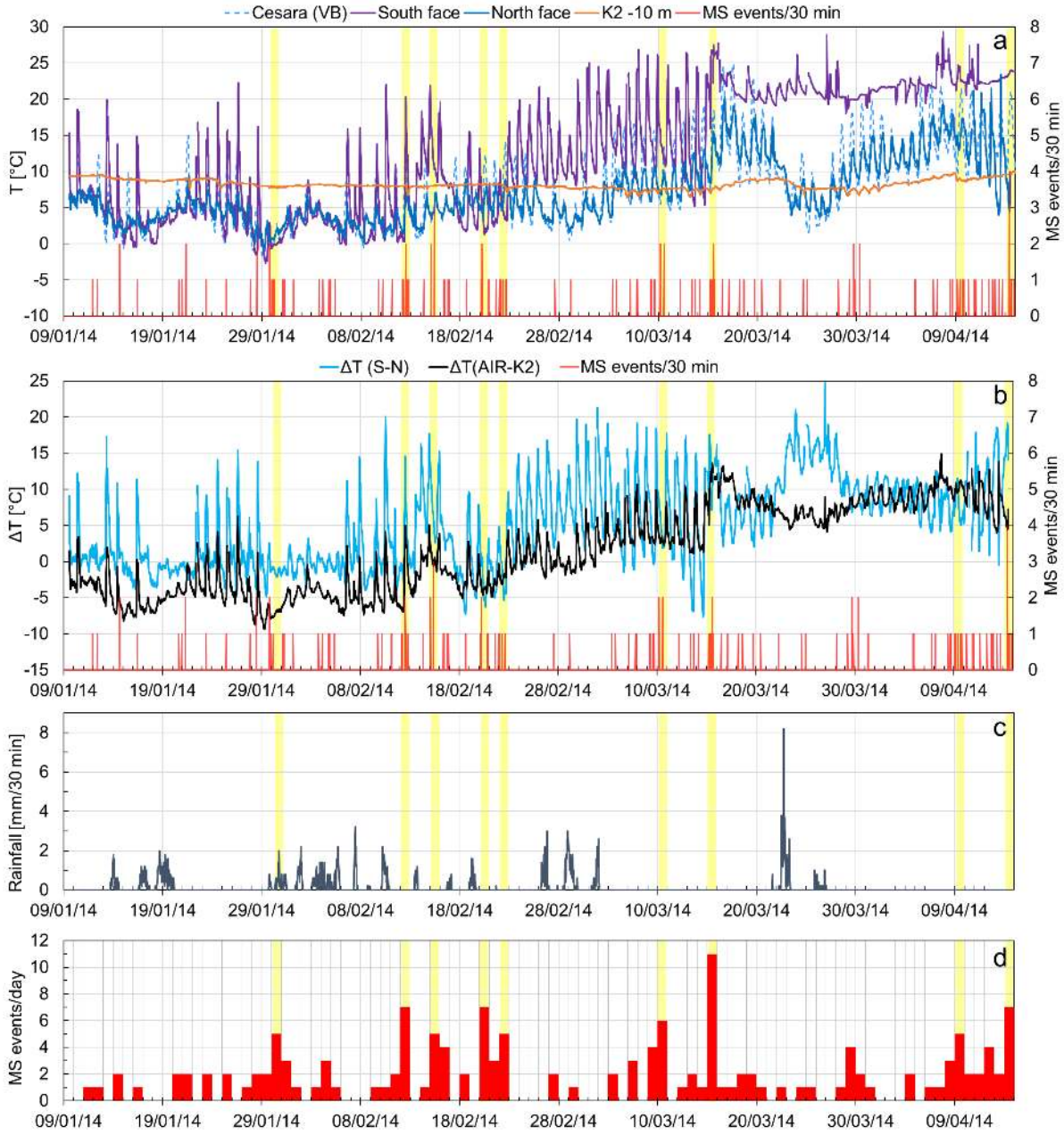

Figure 4 (a) 30-minute air temperature recorded on site by three on-site temperature probes (north face, south face, 10-m depth in fracture K2) and the reference meteorological station of Cesara (ARPA Piemonte) for the period January-April 2014. (b) Related temperature difference computed between the south and north faces of the cliff and between the average of the two faces and the deep probe in fracture K2. In (a) and (b) the 30-minute MS event rate is shown for comparison. (c) 30-minute rainfalls during the same period, from the meteorological station of Cesara (ARPA Piemonte). (d) Daily MS-event rate. Days with more than 5 MS events are highlighted in all the sections.

In Figure 5 both temperature/rainfalls (in a and c) from the meteorological reference station and MS-event occurrence (in d) are shown for the whole monitored period at simultaneous 30-minute sampling intervals.

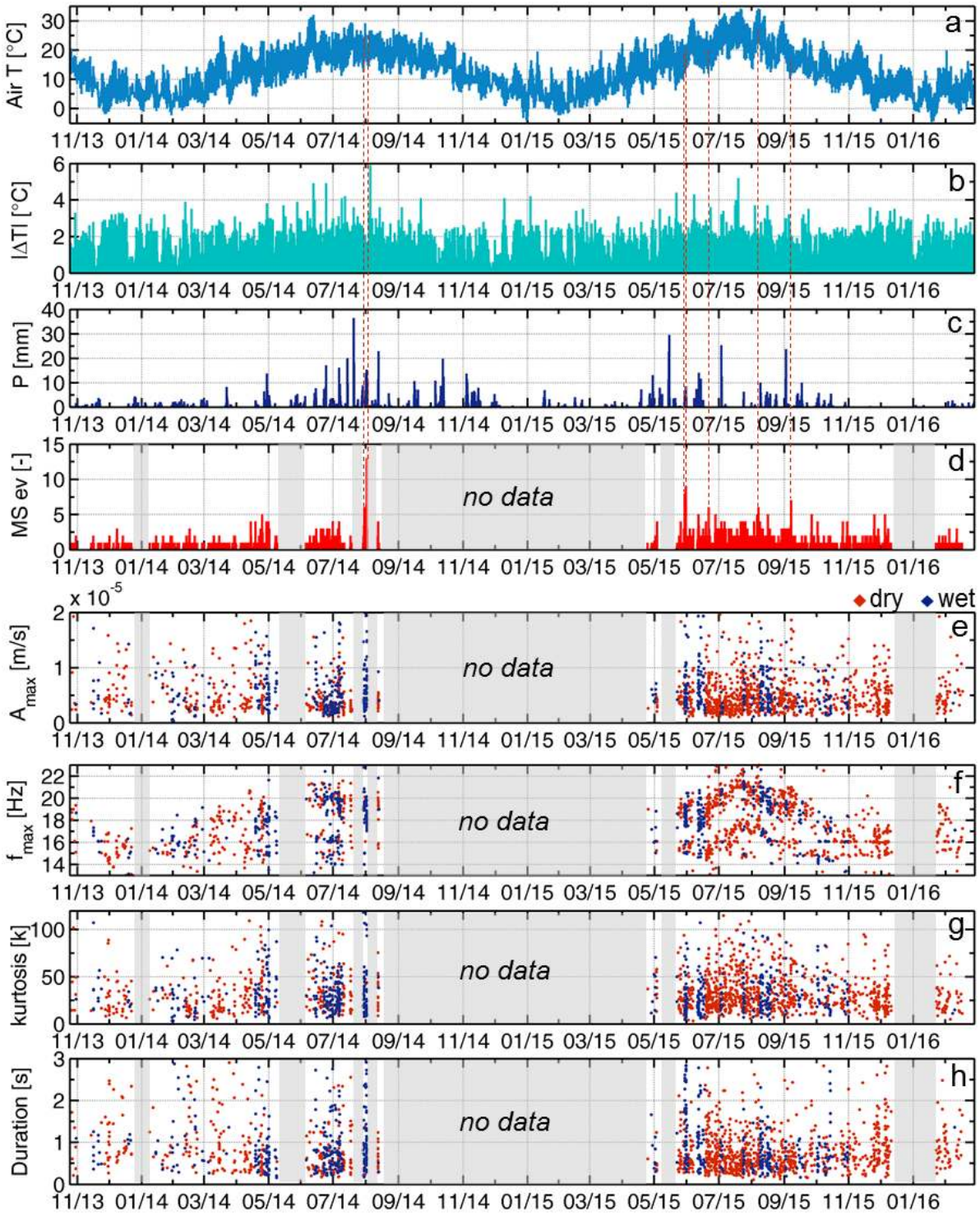

Figure 5 (a) 30-minute air temperature at the meteorological station of Cesara (ARPA Piemonte), in the period November 2013-February 2016. (b) Absolute value of thermal excursion between subsequent 30-minute measurements. (c) 30-minute rainfalls recorded at the same location. (d) 30-minute number of MS events recorded on site. From (a) to (d) vertical red dashed lines highlight the half-hours with more than 5 events (summarized in Table 1). (e) Maximum amplitude, (f) maximum frequency peak, (g) kurtosis and

(h) duration of the recorded MS events (parameters of the events recorded in dry and wet conditions are reported in red and blue respectively).

Unfortunately, no information on the temperature difference between the two faces of the cliff was retrieved. The absolute temperature difference of each half-hour with respect to the previous, is shown in Fig. 5b to globally highlight marked air temperature fluctuations. The computed half-hour average temperature excursion is ±0.4°C.

All the detected seven half-hours exceeding 5 MS events (summarized in Table 1) are located in warm months. Six of these peaks are recorded at night or in late afternoon. Most of the peaks are related to temperature differences (recorded during the half-hour or in the previous 30 minutes) higher than the average value computed over the whole period. Additionally, comparing Figure 5b and Figure 5d, half-hours exhibiting more than 4°C of temperature variations are always accompanied by microseismicity, even if the number of events does not always exceed 5 events/hour. The increase in MS activity along the whole monitored period is therefore confirmed to be related to sudden thermal variations.

Four of the main peaks (Table 1) are associated to rainfalls. The highest precipitation peak (14 mm) also corresponds to the maximum MS-event occurrence (13 events). Comparing Figure 5c and Figure 5d, the highest MS peaks are found after intense or long-lasting periods of precipitation. This fact partially contrasts with what observed in the shorter time window related to the cold months (Fig. 4). Taken together, these observations suggest a combined contribution of temperature (difference and increase) and rainfall to the microseismicity of the site.

Characterizing parameters of the recorded MS events are summarized in Figure 5 (e to h), in order to investigate possible variations in maximum amplitude, frequency peak in the Fourier spectrum, kurtosis, and duration between events occurring in dry or wet conditions. The threshold to distinguish events occurring in wet conditions was fixed to a minimum of 5 mm of rain cumulated within 2 days before the event start time. No significant changes in the parameters are observed between events occurring in dry or wet conditions. Conversely, a strong air temperature control on the peak frequencies in the Fourier spectra of the recorded events (Fig. 5g) is identified, as already highlighted for ambient noise resonance frequencies in *Colombero et al.* [2017]. Air temperature and frequency fluctuations are almost in phase, with maximum frequency during the hottest hours and lower values in cold periods. Maximum-amplitude and kurtosis values seem to be weakly correlated to temperature fluctuations also.

Table 1 30-minute time windows showing clusters of more than 5 MS events and related relationship with the rainfall amount and temperature variations in the half hour before and after the reported start time.

Date [dd/mm/yyyy]	**Start Time [hh:mm:ss]**	**MS events/ 30 min**	**Rainfall/ 30 min [mm]**	**ΔT_{ST-30} [°C]**	**ΔT_{ST+30} [°C]**
31/07/2014	17:00:00	6	8	-1	+0.6
01/08/2014	00:30:00	13	14	-0.2	-0.6
29/05/2015	21:00:00	8	5	-1.4	0

31/05/2015	01:00:00	9	8	-0.4	+0.8
21/06/2015	21:30:00	6	0	-0.6	-1
08/08/2015	01:30:00	6	0	0	-0.8
07/09/2015	13:30:00	7	0	+1.8	-0.4

3 Microseismicity at the laboratory scale

3.1 Equipment and experimental conditions

Since temperature variations and gradients within the rock mass were recognized to be the main potential governing factors of the site microseismicity, laboratory tests were designed to investigate thermal effects on fractures, under controlled boundary conditions. With this aim, intact rock samples of *Granito di Alzo* were selected from a quarry nearby the test site, to perform after-rupture temperature ramps, using concomitant AE recordings as a proxy to field-scale MS data. The experiments were conducted both in dry and saturated conditions, to further explore the influence of fluids on the sample behavior during the heat treatment.

The experimental setup consists of a servo-controlled triaxial apparatus (TRI-X 100 MPa/200°C, Sanchez Technologies) with an actuator providing axial stress (σ_1, up to 680 MPa), and with confining pressure ($\sigma_2=\sigma_3$, up to 100 MPa) applied via silicone oil using syringe pumps. An independent pressurization system controls the pore pressure for sample saturation. An external furnace applies temperatures up to 200°C. The sample consists of a cylindrical intact rock sample of 40-mm diameter and 100-mm length separated from the confining medium by an engineered rubber jacket [*Sammonds*, 1991]. The jacket is fitted with 12 ports for installing an array of 12 piezoelectric transducers (1-MHz central frequency) to record the AE activity during the test (at a sampling frequency of 10 MHz). The system was also set to perform an active survey across the sample every 2 minutes by pulsing each of the 12 sensors in sequence with a 200-V pulse whilst the remaining 11 function as receivers. The waveforms of each survey were stored to enable first arrival time picking and the construction of the evolving velocity model of the sample, a fundamental requirement for hypocenter location of the detected AEs.

The first preliminary test phase involved generation of fractures within all the samples. Samples were deformed until rupture at a constant axial strain rate of $5 \cdot 10^{-6}$ s^{-1}, controlled via linear variable displacement transducers (LVDTs). Two type of experiments were carried out: 'dry' tests, i.e. confining pressure of 2 MPa and no pore pressure (samples G1, G2 and G5), and 'wet' tests, i.e. water saturated experiments with a constant pore fluid pressure (de-ionized/distilled water) of 0.5 MPa, and a confining pressure of 2.5 MPa (samples G3 and G4). We note that laboratory loading conditions during this phase are different from the site conditions which have led to fracture formation. This laboratory test phase was necessary to obtain fractures within the samples and to obtain reference AE waveforms and spectrograms of the microcracking processes to validate the AE waveforms of the second phase. Even given the different failure conditions between laboratory and site during this phase, confining pressures were kept low (2 MPa, approximately 80 m depth) to reflect the near-surface circumstances in which fractures could probably have formed.

After failure, the post-failure differential stress (σ_1-σ_3) was set to the 75% of its residual value, to reduce marked loading conditions and enable possible thermal expansion both in axial and radial directions. Setting the differential stress to a constant value for the thermal stages of the tests had the advantage to allow the sample to freely equilibrate according to the applied thermal variations and to balance and control its deformation, in order to avoid the test failure. Maintaining these conditions, the two samples were then heated from room temperature (~27°C) up to 65°C. Temperature was applied to the upper surface of the cylindrical samples, and progressively propagated within the sample volume. Measurements at the top and bottom surfaces of the samples were performed every 3 seconds (same sampling rate of the mechanical parameters), thus providing an estimation of the thermal gradient across the sample during the whole test duration. Both samples were maintained at the upper target temperature for 15 minutes and then left to cool down to the original ambient temperature. The heating rate was +0.4°C/min from room temperature to 50°C for both samples, followed by +0.15°C/min for the dry (G5) test and +0.2°C/min for the wet (G4) test from 50°C to 65°C. Both samples cooled down to room temperature at an average rate of -0.15°C/min. Due to technical limitations, it was not possible to test the samples at temperature lower than the room temperature, to have a full comparison with the range of temperature variations detected on site.

3.2 AE processing methods

Similarly to field MS dataset, AE processing firstly involved spectral analysis and source location of the recorded waveforms. AE source location was attempted to compare a representative dataset of events occurring during both the failure and heating stages of the dry (G5) and wet (G4) tests. The evolving velocity model of each sample was reconstructed from the active surveys performed every 2 minutes across the specimens during the whole duration of the tests. A transversely isotropic simplex location algorithm was used for the AE events showing accurate first-arrival-time picking on at least 6 of the 12 recording channels.

In addition, the same parameters computed for the MS events (maximum amplitude, frequency peak in the AE-event Fourier spectrum, kurtosis and duration) were computed for all the AEs having a clear onset on at least 6 channels, in order to avoid disturbances and transients. Analyses on the temporal variation of these parameters as a function of external factors (stress drop and temperature) were undertaken to gain insight on the sample behavior and to provide comparison and support to the interpretation of the field-scale microseismicity.

3.3 AE dataset: spectrograms and source location

Stress-strain curves for the five experiments are shown in Figure 6a. For the water-saturated samples (G3 and G4), a lower strength is noted at approximately 130 MPa compared to the dry samples G1 and G2 of approximately 150 MPa axial stress. These results highlight a strength reduction driven by water, which enhances crack nucleation and propagation. A slightly different behavior is evident for sample G5, which exhibited a minor peak before the final failure and a significantly lower peak strength (maximum axial stress of less than 90 MPa). This behavior is likely due to pre-existing fractures within the sample, which contributed to significantly decrease its final strength, and is considered an outlier to the set. However, such heterogeneity can also serve as evidence of the fracturing conditions of the investigated rock mass.

AE hit rates throughout the tests are compared in Figure 6 (c and e, respectively) for samples G5 (dry) and G4 (wet). Thermal conditions along the test phases are reported in Figure 6b and Figure 6d in terms of temperature values at the top and bottom surfaces of the samples, and temperature difference between the two faces. In the preliminary failure stage of both tests, as peak stress and sample failure were approached, the AE-hit rate increased entering the supra-exponential phase [described by *Benson et al.,* 2007]. After failure, the AE-hit rate entered a period of quiescence (e.g. 2000-3500 s for G5) until the heating stage was activated. At this point, the AE activity picks up dramatically after 5000 s for sample G5 (Fig. 6b). The AE peaks also corresponds to the time at which the maximum temperature difference is measured between the two edges of the samples (16°C). This observation may indicate temperature-driven new microcracking of the sample. By contrast, fewer events are detected during the cooling stage as seen from approximately 14000 s in G5 and during both the heating/cooling stages of sample G4 (Fig. 6c).

During the tests, subtle but clear changes in the spectral content of the waveforms were also noticed. These are summarized for the different test phases in Figure 7 (failure stage), Figure 8 (initial heating stage, from room temperature to approximately 45°C) and Figure 9 (initial cooling stage, from 65°C to 50°C) as a function of either differential-stress (for the failure stage at constant temperature) or temperature fluctuations (for the heating and cooling stage at constant differential stress).

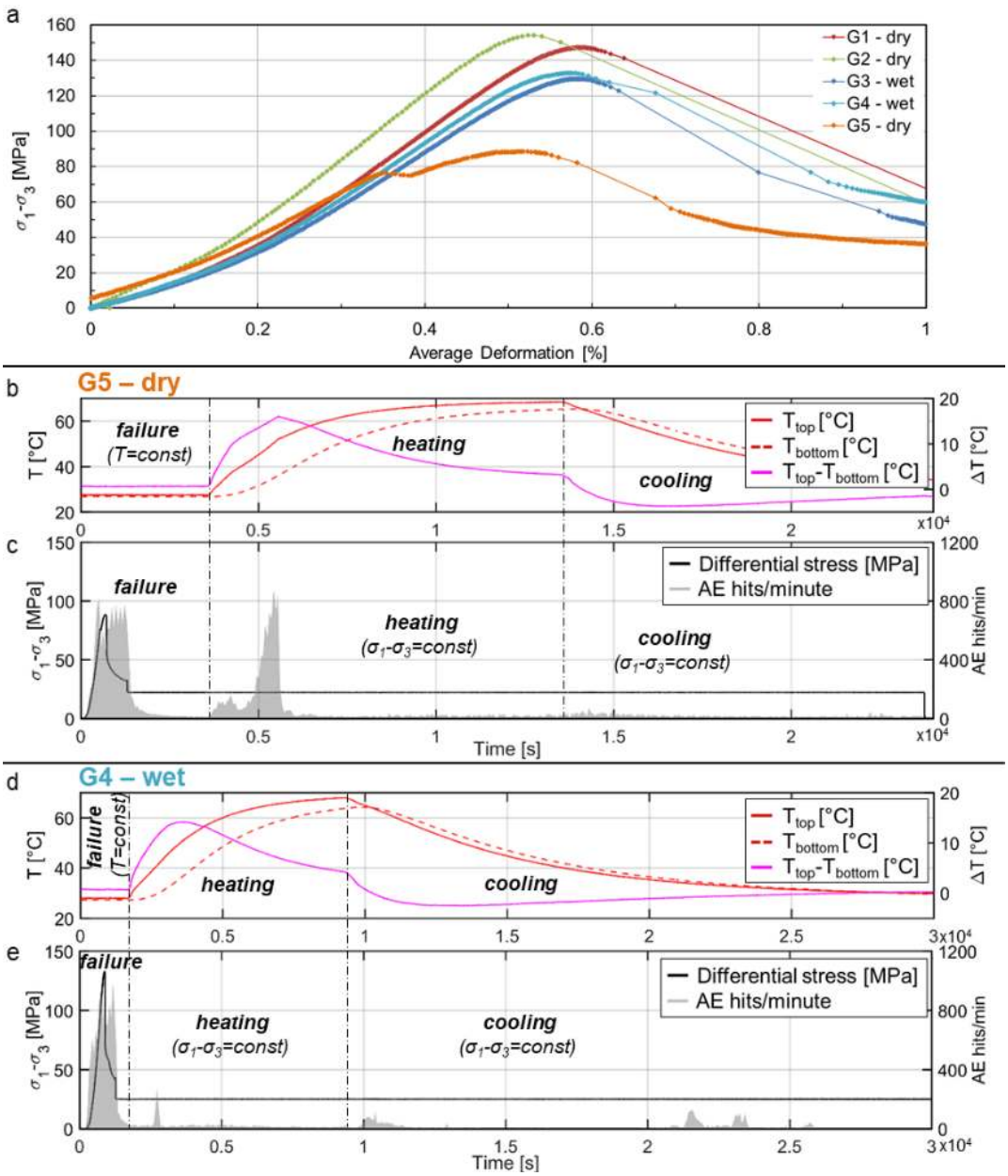

Figure 6 (a) Stress-strain curves from the preliminary failure stages of all the tested samples. (b-c) G5 dry test: (b) Temperature of the top and bottom surfaces of the sample and related temperature difference; (c) Differential stress and AE-hit rate during the test. (d-e) G4 wet test: (d) Temperature of the top and bottom surfaces of the sample and related temperature difference; (e) Differential stress and AE-hit rate during the test.

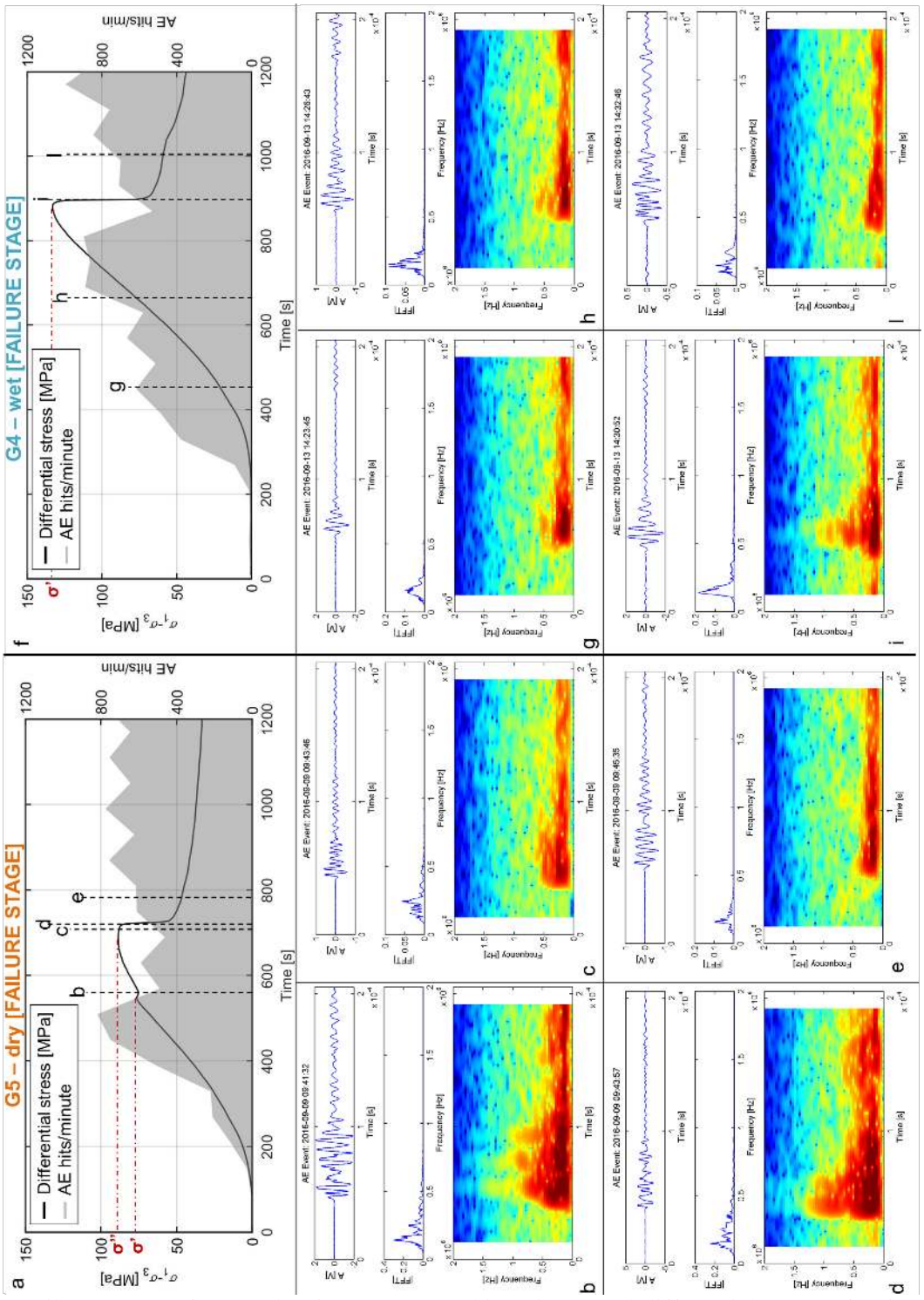

Figure 7 Failure stages of G4 and G5 tests. (a) AE hits/minute and differential stress of G5 test (dry). From (b) to (e), selected representative AE events (waveform, Fourier spectrum and spectrogram, from the top to the bottom of each section), event occurrence time is highlighted in (a) with the vertical black dashed lines. (f) AE hits/minute and differential stress of G4 test (wet). From (g) to (l), selected representative AE events (waveform, Fourier spectrum and spectrogram, from the top to the bottom of each section), event occurrence time is highlighted in (f) with the vertical black dashed lines. The temperature is constant (room temperature) during the failure stages of both tests.

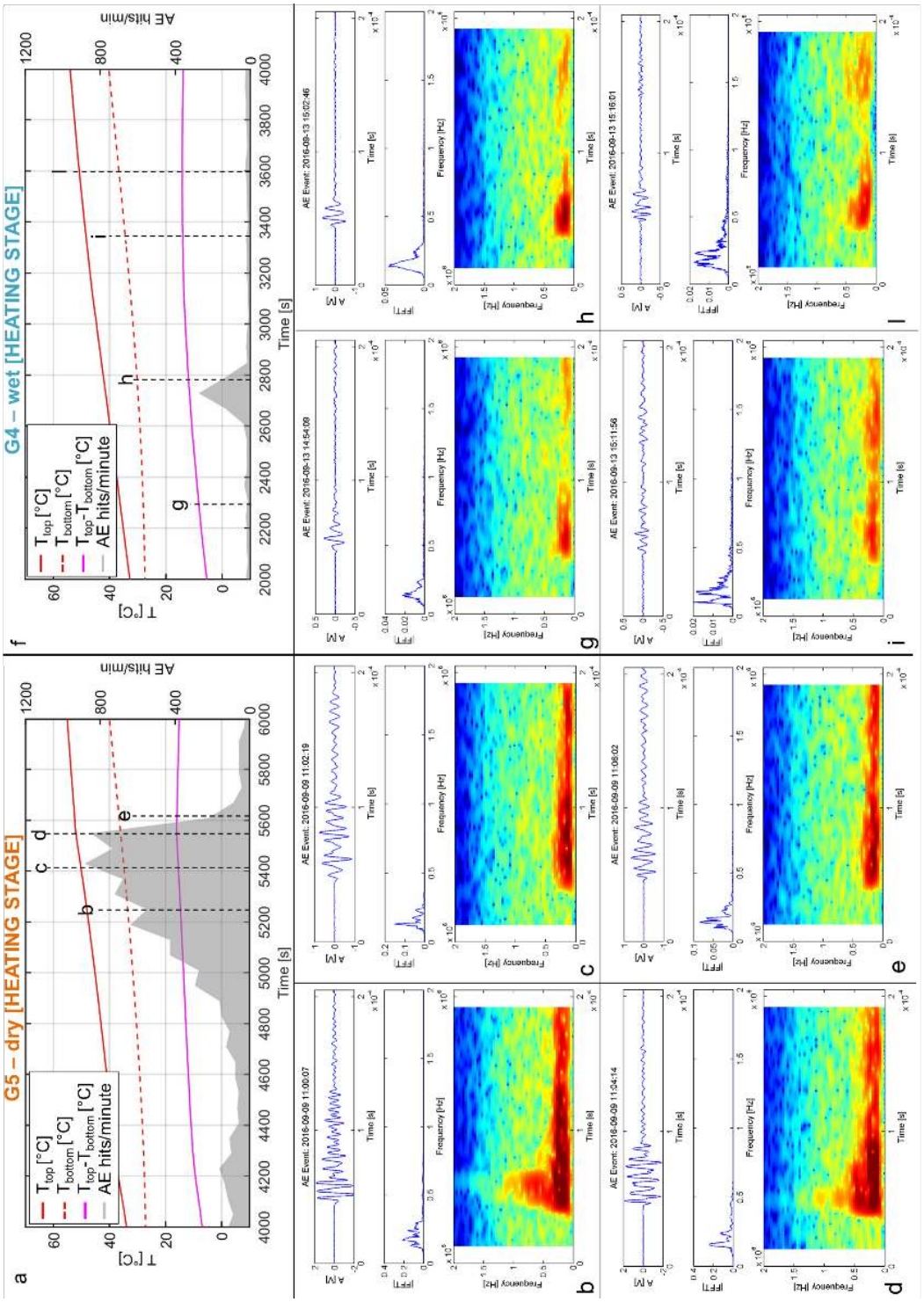

Figure 8 Heating stages (from room temperature to 40°C) of G4 and G5 tests. (a) AE hits/minute and sample temperatures of G5 test (dry). From (b) to (e), selected representative AE events (waveform, Fourier spectrum and spectrogram, from the top to the bottom of each section), event occurrence time is highlighted in (a) with the vertical black dashed lines. (f) AE hits/minute and sample temperatures of G4 test (wet). From (g) to (l), selected representative AE events (waveform, Fourier spectrum and spectrogram, from the top to the bottom of each section), event occurrence time is highlighted in (f) with

the vertical black dashed lines. The differential stress is constant (75% of the residual value after failure) in both tests.

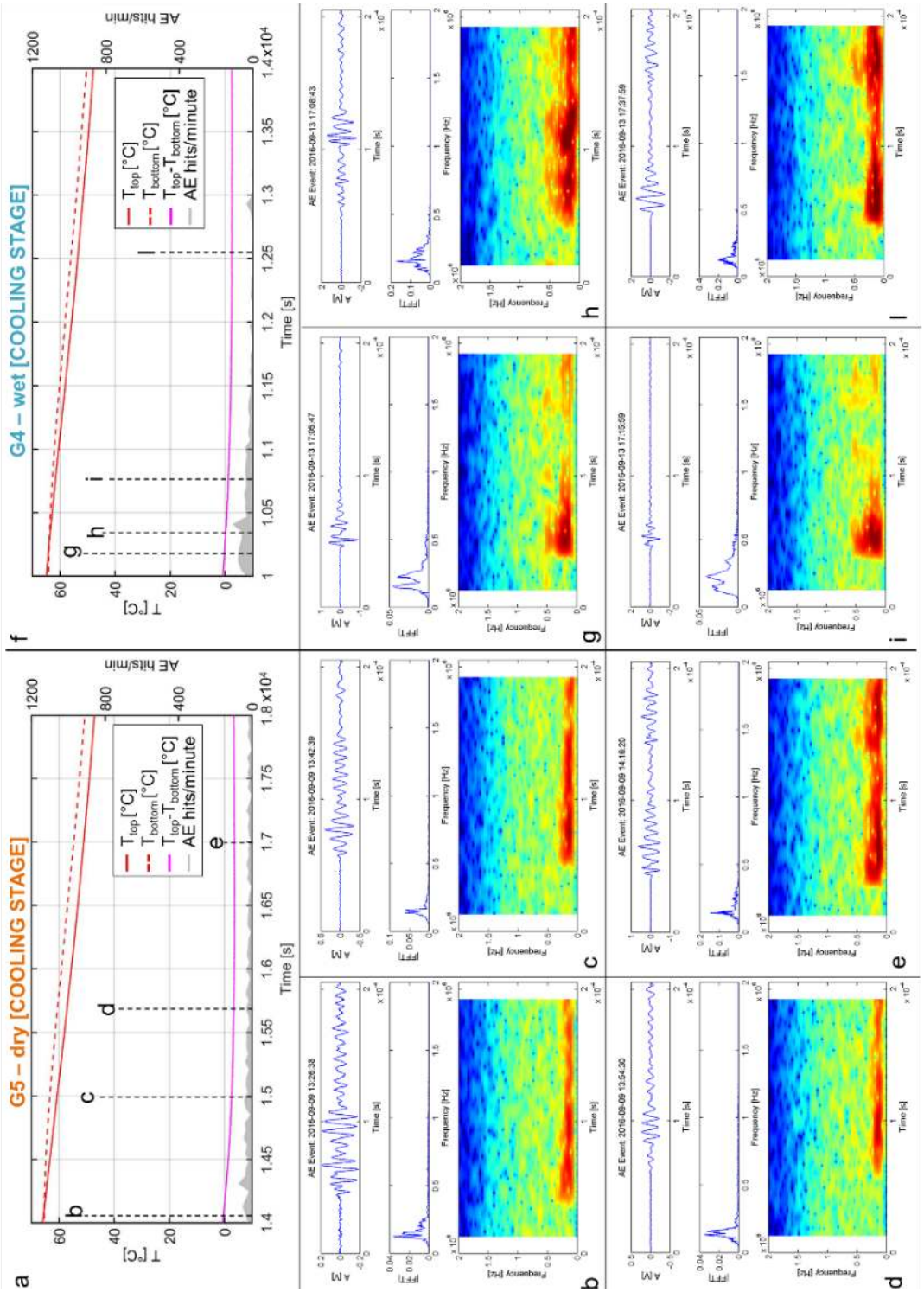

Figure 9 Cooling stages (from 65°C to 50°C) of G4 and G5 tests. (a) AE hits/minute and sample temperatures of G5 test (dry). From (b) to (e), selected representative AE events (waveform, Fourier spectrum and spectrogram, from the top to the bottom of each section), event occurrence time is highlighted in (a) with the vertical black dashed lines. (f) AE hits/minute and sample temperatures of G4 test (wet). From (g) to (l), selected representative AE events (waveform, Fourier spectrum and

spectrogram, from the top to the bottom of each section), event occurrence time is highlighted in (f) with the vertical black dashed lines. The differential stress is constant (75% of the residual value after failure) in both tests.

In the failure stage of the dry test (Fig. 7a), approximately the 60% of the recorded AEs show a high-frequency onset (e.g. Fig. 7b and d, hereafter called HF), similar to the MS spectral shapes recorded on site. These are very energetic events, which have been usually linked to fracturing/failure mechanisms driving the cracks growth and linkage into macroscopic fracture surfaces [*Benson et al.*, 2010]. In the remaining 40% of the recorded dataset, the high-frequency onset is partially missing (e.g. Fig. 7c), as also observed on site (Fig. 2c and d), but still reflects the HF reference spectral shape. After failure, all the recorded events are low-frequency AEs (hereafter called LF, e.g. Fig. 7e) which may be linked to stick-slip along the generated macro-fractures. In contrast, during the failure stage of the wet test (Fig. 7f), with the exception of the clear HF AEs related to the final failure (Fig. 7i), more than 95% of the recorded signals show less pronounced high-frequency onsets (e.g. Fig. 7g and h). These spectrograms are more akin to the LF frictional signals observed in the stick-slip after failure (Fig. 7l) and can be explained as 'hybrid' events, with a less pronounced onset and a long lasting tail, caused by a combination of the opening of new cracks and pathways with the movement of the high-pressure pore fluid [*Benson et al.*, 2010].

Many new HF events are recorded during the heating stage (Fig. 8a) of the dry test (e.g. Fig. 8b and d). These spectral shapes are common to approximately the 40% of the AEs recorded during the AE peak at 5000-5500 s. The remaining events show LF spectral shapes (e.g. Fig. 8c and e). They represent approximately the 60% of the detected AEs during the AE peak and become the only dominant spectral shapes after it. Conversely, only a reduced number of LF events is recorded during the heating (Fig. 8f) of the wet sample (Fig. 8g to l) with no associated HF events.

No HF type events are detected during the cooling stage of the dry sample (Fig. 9a to e), while spectrograms of the wet sample (Fig. 9f to l) are similar to the failure stage and could potentially indicate new damage within the sample.

The AE source location was obtained for 468 events of the dry test and 282 events of the wet test. Particularly, for the dry test, 258 located events are related to the initial failure stage (HF AEs) and 210 to the heating stage (73 AEs showing HF spectrograms and 137 AEs with LF spectral content). For the wet test, 222 and 50 located events were related to the failure and heating stages respectively (with only 8 AEs showing HF features during the failure phase). As highlighted in Figure 10, complex fracture systems are generated from the deformation/failure process on both samples, roughly consisting in a conjugate system of two main fractures, with associated several micro-fractures. During the dry test (Fig. 10a to d), failure-related AEs appear to originate within the most fractured areas, with two main clusters of events, roughly separated and centered along the vertical axis, in the lower and upper half of the sample respectively. Heating-related AE sources are mainly located between these two clusters. For the wet test (Fig. 10e to h), a weaker correlation with the location of the macroscopic fracture traces is observed both for the failure- and heating-related events. This is likely to reflect the more intense pervasive microfracturing of the saturated sample driven by water flow.

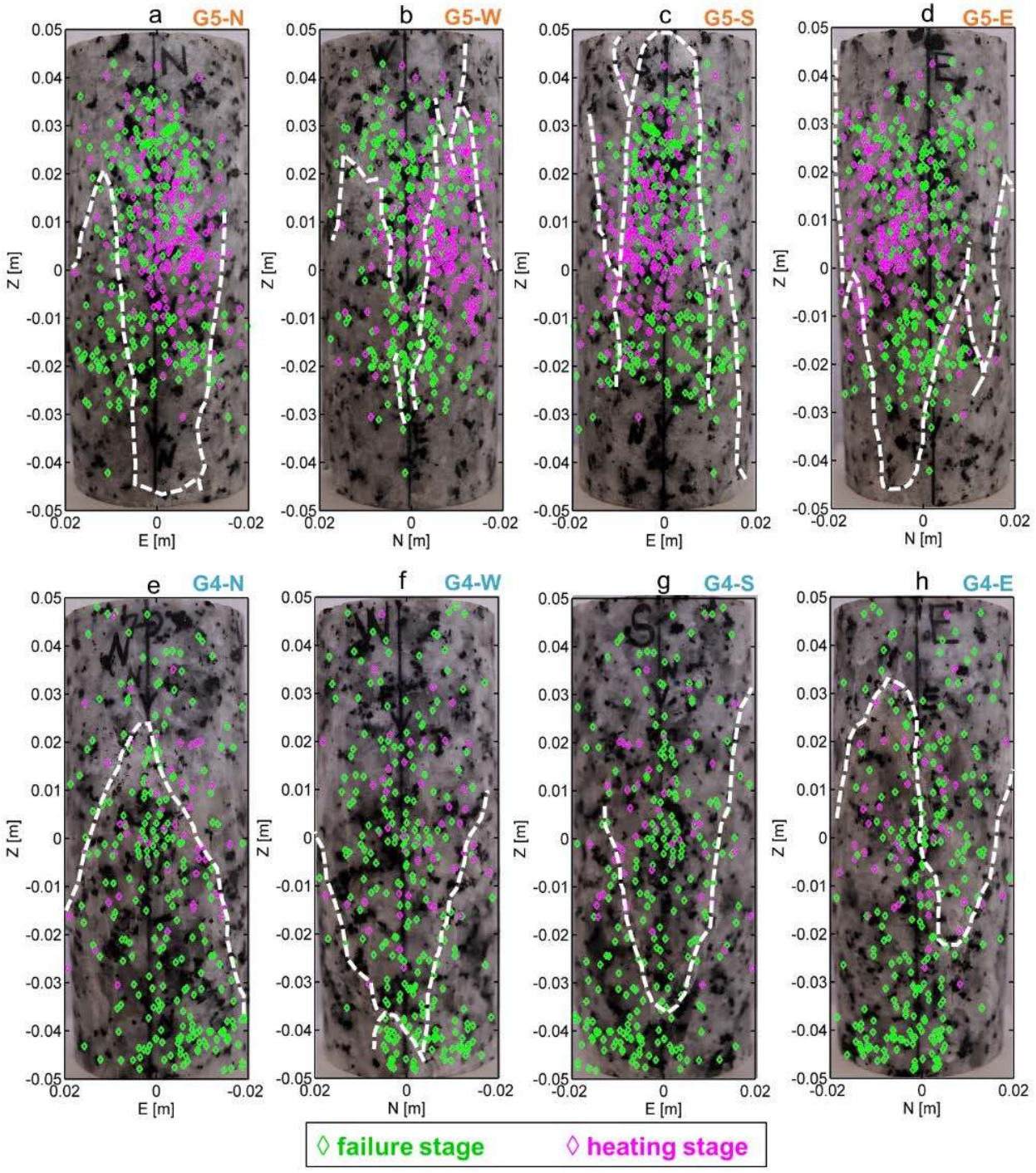

Figure 10 AE-event location. (a-d) G5 dry sample, view of the 468 relocated events from the (a) north, (b) east, (c) south and (d) west face. (e-h) G4 wet sample, view of the 332 relocated events from the (e) north, (f) east, (g) south and (h) west face. Green and magenta diamonds refer to the events occurred during the failure and heating stage of each test respectively. On each sample face, the macroscopic fracture traces are highlighted with the dashed lines.

3.3 AE dataset: correlation with external factors

In order to gain further insight on the sample behavior, the same salient parameters computed for the MS field dataset have been analyzed for the laboratory AEs, as a function of the external factors (stress drop and temperature) applied during the tests. AE maximum amplitudes, frequency peaks in the Fourier spectrum, kurtosis and duration values are reported in Figure 11 for the failure stage and in Figure 12 for the heating/cooling stages of both the dry and wet experiments.

During the dry test, AE maximum amplitude is found to increase approaching both the first and the main stress drop related to the sample failure (related differential stresses are indicated with σ' and σ'' respectively in Fig. 11a). After failure, lower amplitude values are found for the LF events associated to the post-failure stick slip. A new amplitude increase characterizes the beginning of the heating stage, most probably due to the formation of new micro-cracks, until probable fracture sealing caused by the thermal expansion of the sample (around t=5500 s from G5 test start time, corresponding to maximum temperature difference between the sample edges=16°C, Fig. 12a). After this peak, the temperature gradient starts to decrease, and high AE amplitudes are no longer detected, even during the cooling stage. Only a few low-amplitude signals are recorded, probably due to gouge crushing and comminution linked to fracture closing/opening. The frequency behavior over time is even more significant in differentiating these two phenomena (Fig. 11b). Before the first stress drop (σ'), frequency peaks of the HF AEs cluster around the mean values of both 242 kHz (highlighted with f', in Fig. 11b) and 154 kHz (f'', in Fig. 11b). After σ', frequency peaks focused around f' almost disappear. After the main stress drop (σ'') frequency peaks are centered around an even lower residual value (f_{RD} = 140 Hz, in Fig. 11b). In the first heating stages, a new concentration of HF AEs is observed around f' and f'', while after fracture sealing, the frequency peaks of the remaining few LF AEs remain centered on the residual value f_{RD}. Since kurtosis defines the 'peakedness' of a signal, it may be an additional useful discriminatory parameter between LF stick slip waveforms (long duration and flat shape, with associated low kurtosis) and HF micro-cracking signals (shorter duration and sharper shape, with associated high kurtosis). The highest kurtosis values are recorded before σ'; while are comparable in the time interval between σ' and σ'' (Fig. 11c) and in the heating phase preceding fracture sealing (Fig. 12c). Conversely, the AE durations are minimum before σ' (Fig. 11d) and progressively increase after the first failure. Some events with short duration are detected in the heating stage before fracture sealing, while further heating and cooling events exhibit longer durations (Fig. 12d).

The failure stages of the wet sample showed a similar behavior (Fig. 11e to h). Before failure, frequency peaks are centered on the same f' and f'' average values found from the dry test, even if the majority of events exhibited LF spectral shapes (no high-frequency onset). A clear frequency cut-off is noticed at σ'. After failure, frequency peaks are located around the residual wet value of 127 Hz (f_{RW} in Fig. 11f), thus slightly lower than the dry f_{RD} value (Fig. 11b). No clear clustering of the parameters is observed during the heating/cooling stages of the wet test (Fig. 12e to h). Fluid circulation is therefore likely to have inhibited fracture sealing associated to the sample thermal expansion.

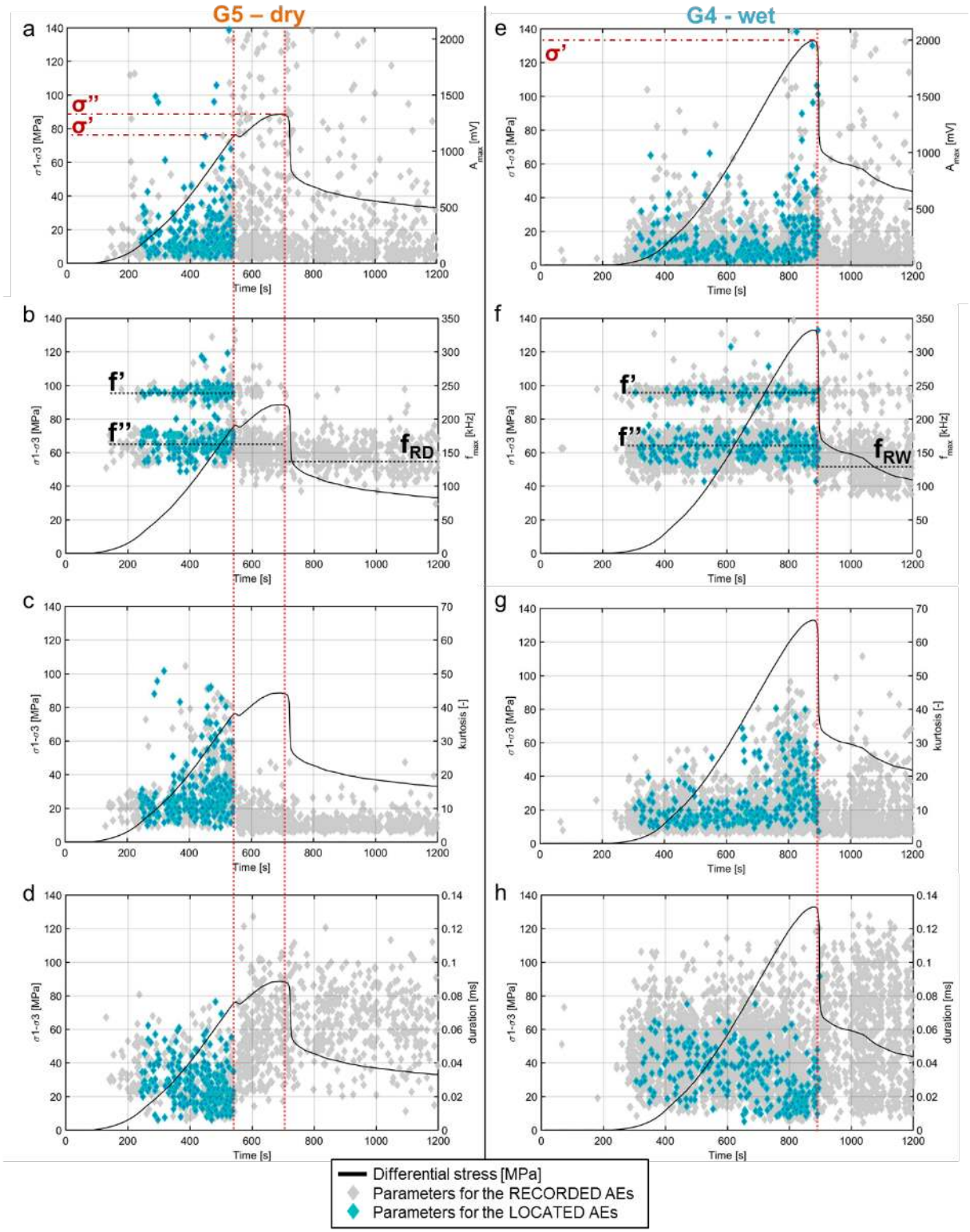

Figure 11 AE parameters during the failure stages of G5 (left column) and G4 (right column) tests. (a, e) Maximum Amplitude; (b, f) maximum frequency peak; (c, g) kurtosis value; (d, h) duration. Gray and light blue diamonds refer to whole AE dataset (events with clear onset on at least 6 channels) and the localized AE events respectively.

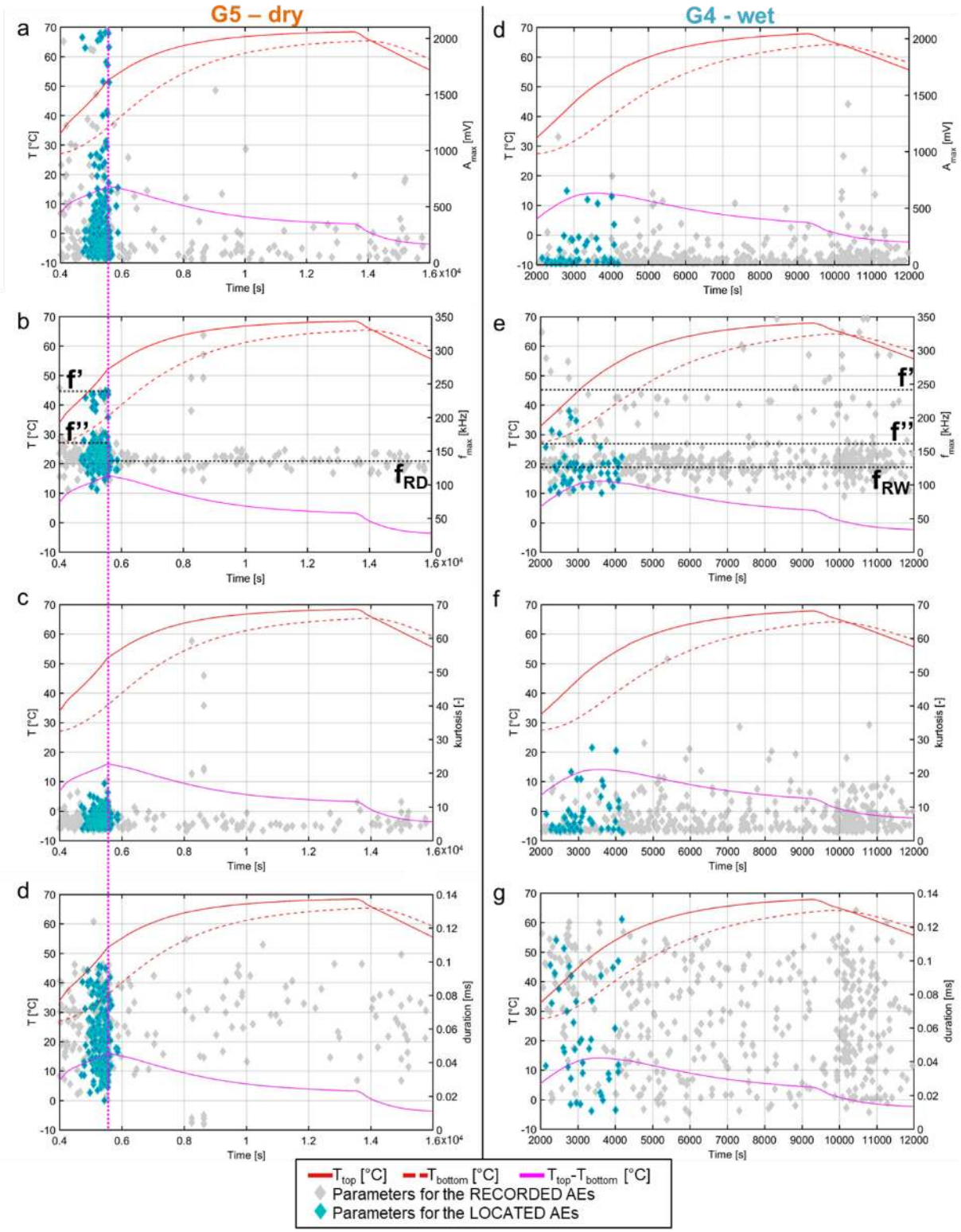

Figure 12 AE parameters during the heating/cooling stages (from room temperature to 65°C/from 65°C to 60°C) of G5 (left column) and G4 (right column) tests. (a, e) Maximum Amplitude; (b, f) maximum frequency peak; (c, g) kurtosis value; (d, h) duration. Gray and light blue diamonds refer to whole AE dataset (events with clear onset on at least 6 channels) and the localized AE events respectively.

4 Discussion and conclusions

Our analysis of the seismic dataset recorded at the potentially unstable cliff revealed the presence of several MS events during the monitored period. Dealing with the site stability, it must be highlighted that the recorded microseismic activity is limited (1773 MS events in almost 18 monitored months) and involves no irreversible acceleration in the MS-event rate. Summer peaks of more than 30 MS events/day are reduced to lower daily rates (around 2-5 MS events/day) in colder months. MS events exhibited peculiar spectral characteristics (HF onset with rapid exponential decay) which have been usually related in literature to micro-cracking processes or small-scale slips along fractures. Source location confirmed that they originate within the rock mass, close to the most pervasive and open fractures.

These results show similarities with the experiments carried out by *Garbini* [2009], *Swami* [2011] and *Warren et al.* [2013] on decimetric granitic boulders. These intact boulders can be considered as a mesoscale unfractured reproduction of the granitic cliff of Madonna del Sasso. Related experimental results found a prominently larger number of AE sources located on the top of the investigated boulders, while very few events occurred in their bottom part. Moreover, in the upper hemisphere of each boulder, the densest hypocentral locations clustered along the east-west central line due to differential insolation of the top-bottom and south-north faces. Interestingly, the observed distribution of MS-event source locations at the cliff scale perfectly compare with these observations. Moreover, similarly to our results, *Swami* [2011] correlated the majority of the recorded events with sudden variations in temperature, caused by either different insolation of the boulder faces (particularly evident in late afternoon and evening hours), or rapid global changes in solar radiation, due to cloud movement or to a modification in the wind speed and direction. These sudden temperature variations caused thermal contraction and expansion of the boulders (measured with independent strain gauges). By analogy with these experiments, it can be therefore confirmed that sudden thermal variations (temporal gradient) or marked temperature differences between the cliff's faces (spatial gradient) may cause differential thermal dilation and induce thermal stresses leading to microcracking processes, as demonstrated by *Gunzburger et al.* [2005].

Considering rainfall and moisture content during the experiment of *Swami* [2011] we notice the largest number of AE events occurred during precipitation, or when the monitored boulder was wet. However, precursor events often preceded the start of rainfall time, probably due to the concomitant meteorological and temperature changes. Coherently, on the longer term, rainwater seems to play a role in promoting microcracking at the studied site, but interpreted only in the direction of inducing or accelerating thermal variations and gradients within the rock mass.

To better focus on the role of temperature in rock fracturing, analogue laboratory tests were performed on samples of the same lithology outcropping at the cliff of Madonna del Sasso. As discussed earlier, some necessary variations between the precise site and laboratory test conditions still remain due to the need of reproducing in a confined cell the near-surface site conditions of an outcropping cliff. The triaxial failure stages of each test were therefore aimed only to the generation of fractures within the samples and to produce reference AEs undoubtedly related to fracturing, for further comparison with the AE waveforms of the heating and cooling stages of the same tests. The failure stage was not indeed intended to reproduce neither the loading site conditions nor the fracture processes occurring within the cliff. A significant AE activity driven by thermal stresses was recorded during the heating phase of the dry sample.

Particularly, the peak of AE occurrence was coincident with the major temperature difference between the two faces of the sample, reflecting site observations. Despite the different scale of observation, and thus the dominant frequency of the events, HF thermal cracking AEs during the preliminary failure stage showed spectral shapes consistent to HF cracking; these compared well to MS-event spectrograms of the field site. This provided the final evidence of the thermal cracking nature of the signals recorded.

The absence of a significant number of LF events, commonly used to indicate fluid or frictional processes, in the field MS dataset further suggests that the main cause driving the microseismic activity at the site is the formation of new micro-cracks caused by thermal expansion or contraction of the rock mass. Consequently, pore-water content and water movement along fractures at the site do not seem to play a major role in the mechanical behavior of the unstable cliff. This final consideration is also confirmed by the spectral and parametric similarities of the MS events recorded at the site during both dry and wet periods. We therefore conclude that it is more likely that the amount of rainwater and the steep morphology of this rock mass do not allow for a significant saturation of the material and related pore fluid/rock matrix interactions. In addition, water movements within the existing fractures are not particularly forced, being open to the surface. In this case, the role of rainfall will enhance any sudden temperature variations on the cliff, therefore accelerating thermal modifications. The combined MS/AE approach here has thus elucidated our understanding of very shallow thermal-related mechanisms driving the microseismic activity at unstable rock masses, here focusing on the site of Madonna del Sasso, trying to bridge the gap between the two investigation scales.

Acknowledgments

This work was partially funded within Progetto d'Ateneo 2012 - SAFER of Università degli Studi di Torino: “Detecting slow deformation signals preceding dynamic failure: a new strategy for the mitigation of natural hazards” (Grant Number: TO_Call2_2012_0057). The reference MS/AE dataset from site monitoring and laboratory tests can be downloaded from https://www.researchgate.net/publication/317951053_MSAE_dataset_Madonna_del_Sasso (DOI: 10.13140/RG.2.2.19397.65763). Please, contact the corresponding author for further material or information on the dataset.

References

Amitrano, D., J. R. Grasso and G. Senfaute (2005), Seismic precursory patterns before a cliff collapse and critical-point phenomena, Geophys. Res. Lett., 32, 8, L08314.

Amitrano, D., M. Arattano, M. Chiarle, G. Mortara, C. Occhiena, M. Pirulli and C. Scavia (2010), Microseismic activity analysis for the study of the rupture mechanisms in unstable rock masses, Natural hazards and earth system sciences, 10(4), 831-841.

Benson, P. M., B. D. Thompson, P. G. Meredith, S. Vinciguerra, and R. P. Young (2007), Imaging slow failure in triaxially deformed Etna basalt using 3D acoustic-emission location and X-ray computed tomography, Geophys. Res. Lett., 34, L03303, doi:10.1029/2006GL028721.

Benson, P. M., S. Vinciguerra, P. G. Meredith, and R. P. Young (2008), Laboratory simulation of volcano seismicity, Science, 322(5899), 249–252.

Benson, P. M., S. Vinciguerra, P. G. Meredith, and R. P. Young (2010), Spatio-temporal evolution of volcano seismicity: A laboratory study, Earth Planet. Sci. Lett., 297(1), 315–323.

Boriani, A., L. Burlini and R. Sacchi (1990), The Cossato-Mergozzo-Brissago line and the Pogallo line (Southern Alps, N-Italy) and their relationship with the late-Hercynian magmatic and metamorphic events, Tectonophysics, 182, 91–102.

Boriani, A., and E. Giobbi (2004), Does the basement of western Alps display a tilted section through the continental crust? A review and discussion. Per. Mineral., 73, special issue 2, 5–22.

Browning, J., P. Meredith, and A. Gudmundsson (2016), Cooling dominated cracking in thermally stressed volcanic rocks, Geophys. Res. Lett., 43, 8417–8425, doi:10.1002/ 2016GL070532.

Burdine, N. (1963), Rock failures under dynamic loading conditions, Society of Petroleum Engineers Journal, 3, 1-8.

Burlini, L., S. Vinciguerra, G. Di Toro, G. De Natale and J.-P. Burg (2007), Seismicity preceding volcanic eruptions: new experimental insights, Geology, 35(2), 183-186.

Caplan-Auerbach, J., and C. Huggel, 2007 Precursory seismicity associated with frequent, large ice avalanches on Iliamna volcano, Alaska, J. Glaciol., 53(180), 128-140.

Collins, D. S., W. S. Pettitt, and R. P. Young (2002), High-resolution Mechanics of a Microearthquake Sequence, Pure appl. geophys., 159, 197-219.

Colombero, C., C. Comina, G. Umili and S. Vinciguerra (2016), Multiscale geophysical characterization of an unstable rock mass, Tectonophysics, 675, 275-289, doi:10.1016/j.tecto.2016.02.045.

Diodati, P., F. Marchesoni and S. Piazza (1991), Acoustic emission from volcanic rocks: an example of self-organize criticality, Phys. Rev. Lett., 67, 2239-2242.

Eppes, M. C., L. McFadden, K. Wegmann and L. Scuderi (2010), Cracks in desert pavement rocks: further insights into mechanical weathering by directional solar heating, Geomorphology, 123, 97-108.

Fazio, M., P. M. Benson, and S. Vinciguerra (2017), On the generation mechanisms of fluid-driven seismic signals related to volcano-tectonics, Geophys. Res. Lett., 44, 734–742, doi:10.1002/2016GL070919.

Gambino, S. P., A. Mostaccio, D. Patanè, L. Scarfi, and A. Ursino (2004), High-precision locations of the microseismicity preceding the 2002–2003 Mt. Etna eruption, Geophys. Res. Lett., 31, 18, L18604.

Garbini, J. (2009), Instrumentation and analysis of the diurnal processes affecting a natural boulder exposed to a natural environment, UNC Charlotte Thesis, 148 pp.

Gariano, S. L. and Guzzetti F. (2016), Landslides in a changing climate, Earth-Science Reviews, 162, 227-252.

Gunzburger, Y., V. Merrien-Soukatchoff, and Y. Guglielmi (2005), Influence of daily surface temperature fluctuations on rock slope stability: case study of the Rochers de Valebres slope (France), Int. J. Rock mech. Min. Sci., 42, 331-349.

Halsey, D. (1996), The Weathering of Sandstone, with Particular Reference to Buildings in the West Midlands, UK, PhD Thesis, University of Wolverhampton.

Hardy, H. R. (2003), Acoustic emission/microseismic activity – Principles, Techniques and Geotechnical Applications, A. A. Balkema, Lisse, The Netherlands.

Helmstetter, A., and S. Garambois (2010), Seismic monitoring of Séchilienne rockslide (French Alps): Analysis of seismic signals and their correlation with rainfalls, J. Geophys. Res., 115 (F3), F03016.

Lévy, C., L. Baillet, D. Jongmans, P. Mourot and D. Hantz (2010), Dynamic response of the Chamousset rock column (Western Alps, France), J. Geophys. Res., 115, F04043.

Lévy, C., D. Jongmans and L. Baillet (2011), Analysis of seismic signals recorded on a prone-to-fall rock column (Vercors massif, French Alps), Geophys. J. Int., 186, 296-310.

Lockner, D. A., Byerlee, J. D., Kuksenko, V., Ponomarev, A., and A. Sidorin (1991), Quasi-static fault growth and shear fracture energy in granite, Nature, 350, 39-42.

Lomax, A., J. Virieux, P. Volant and C. Berge (2000), Probabilistic earthquake location in 3D and layered models: Introduction of a Metropolis-Gibbs method and comparison with linear locations, in Advances in Seismic Event Location, edited by C. H. Thurber and N. Rabinowitz, Kluwer, Amsterdam, pp.101-134.

McFadden, L. D., M. C. Eppes, A. R. Gillespie and B. Hallet (2005), Physical weathering in arid landscapes due to diurnal variation in the direction of solar heating, Geological Society of America Bulletin, 110, 161–173.

McKay, C. P., J. L. Molaro and M. M. Marinova (2009), High-frequency rock temperature data from hyper-arid desert environments in the Atacama and the Antarctic Dry Valleys and implications for rock weathering, Geomorphology, 110, 182–187.

Moores, J. E., J. T. Pelletier and P. H. Smith (2008), Crack propagation by differential insolation on desert surface clasts, Geomorphology, 102, 472-481.

Paranunzio, R., F. Laio, G. Nigrelli and M. Chiarle (2015), A method to reveal climatic variables triggering slope failures at high elevation, Nat. Hazards, 76, 1039–1061.

Sammonds, P. R. (1999), Understanding the fundamental physics governing the evolution and dynamics of the Earth's crust and ice sheets, Philos. Trans. R. Soc. London, 357(1763), 3377–3401.

Senfaute, G., A. Duperret and J. Lawrence (2009), Micro-seismic precursory cracks prior to rockfall on coastal chalk cliffs: a case study at Mesnil-Val, Normandie, France, Nat. Hazards Earth Syst. Sci, 9(5), 1625-1641.

Spillmann, T., H. Maurer, A. G. Green, B. Heincke, H. Willenberg and S. Husen (2007), Microseismic investigation of an unstable mountain slope in the Swiss Alps, J. Geophys. Res., 112(B7), B07301.

Swami, S. G. (2011), Temperature, strain and acoustic emission monitoring of a natural boulder exposed to the sun: a test on the efficacy of insolation on physical weathering, UNC Charlotte Thesis, 148 pp.

Thompson, B. D., R. P. Young, and D. A. Lockner (2009), Premonitory acoustic emission and stick-slip in natural and smooth-faulted Westerly granite, J. Geophys. Res., 114, B02205, doi:10.1029/2008JB005753.

Walter, M., and M. Joswig (2009), Seismic characterization of slope dynamics caused by soft rock-landslides: The Super-Sauze case study, in Landslide processes: from geomorphic mapping to dynamic modelling, Proceedings of the landslide processes conference, CERG Editions, Strasbourg, France, 215-220.

Warren, K., M.-C. Eppes, S. Swami, J. Garbini and J. Putkonen (2013), Automated field detection of rock fracturing, microclimate, and diurnal rock temperature and strain fields, Geosci. Instrum. Method. Data Syst., 2, 275–288.

Yatsu, E. (1988), The Nature of Weathering: An Introduction, Sozosha, Tokyo, 624 pp.

Young, R. P., and D. S. Collins (2001), Seismic studies of rock fracture at the Underground Research laboratory, Canada, International Journal of Rock Mechanics & Mining Sciences, 38, 787-799.

Figure 1 (a) Geographical location of the test site (Madonna del Sasso), in northwestern Italian Alps. (b) Eastern, (c) Southern and (d) Northern aerial views of the site with indication of fracture traces (K1 to K4) and location of the microseismic stations (ST1 to ST4). The two unstable blocks are highlighted by letters A and B. (e-h) Detail on the microseismic monitoring stations: (e) ST1, (f) ST2, (g) ST3 and (h) ST4.

Figure 2 Examples of microseismic events recorded at Madonna del Sasso. In each section (a-f), from the top to the bottom: seismogram recorded on channel N of ST2, related Fourier spectrum and spectrogram.

Figure 3 MS-event location. (a) 68% confidence ellipsoids referred to the location of 451 MS events. Ellipsoids are plotted in color scale from yellow to red (from surficial to deep events). The center of each ellipsoid is the Gaussian Expectation E(x), marked with the red asterisk. (b) 3-D view of the maximum likelihood solutions (optimum hypocentral location, plotted with red diamonds) for the same events. (c) Daily number of total and located MS events.

Figure 4 (a) 30-minute air temperature recorded on site by three on-site temperature probes (north face, south face, 10-m depth in fracture K2) and the reference meteorological station of Cesara (ARPA Piemonte) for the period January-April 2014. (b) Related average temperature and temperature difference computed between the south and north faces of the cliff and between the average of the two faces and the deep probe in fracture K2. In (a) and (b) the 30-minute MS event rate is shown for comparison. (c) 30-minute rainfalls in during the same period, from the meteorological station of Cesara (ARPA Piemonte). (d) Daily MS-event rate. Days with more than 5 MS events are highlighted in all the sections.

Figure 5 (a) 30-minute air temperature at the meteorological station of Cesara (ARPA Piemonte), in the period November 2013-February 2016. (b) Absolute value of thermal excursion between subsequent 30-minute measurements. (c) 30-minute rainfalls recorded at the same location. (d) 30-minute number of MS events recorded on site. From (a) to (d) vertical red dashed lines highlight the half-hours with more than 5 events (summarized in Table 1). (e) Maximum amplitude, (f) maximum frequency peak, (g) kurtosis and (h) duration of the recorded MS events (dry events, in red; wet events, in blue).

Figure 6 (a) Stress-strain curves from the preliminary failure stages of all the tested samplestriaxial tests. (b--c) G5 dry test: (b) Temperature of the top and bottom surfaces of the sample and related temperature difference; (c) Differential stress and AE-hit rate during the test. (d-e) G4 wet test: (d) Temperature of the top and bottom surfaces of the sample and related temperature difference; (e) Differential stress and AE-hit rate during the test.

Figure 7 Failure stages of G4 and G5 triaxial tests. (a) AE hits/minute, sample temperature and differential stress of G5 test (dry). From (b) to (e), selected representative AE events (waveform, Fourier spectrum and spectrogram, from the top to the bottom of each section), event occurrence time is highlighted in (a) with the vertical black dashed lines. (f) AE hits/minute , sample temperature and differential stress of G4 test (wet). From (g) to (l), selected representative AE events (waveform, Fourier spectrum and spectrogram, from the top to the bottom of each section), event occurrence time is highlighted in (f) with the vertical black dashed lines. The temperature is constant (room temperature) during the failure stages of both tests.

Figure 8 Heating stages (from room temperature to 40°C) of G4 and G5 triaxial tests. (a) AE hits/minute and, sample temperatures and differential stress of G5 test (dry). From (b) to (e), selected representative AE events (waveform, Fourier spectrum and spectrogram, from the top to the bottom of each section), event occurrence time is highlighted in (a) with the vertical black dashed lines. (f) AE hits/minute and , sample temperatures and differential stress of G4 test (wet). From (g) to (l), selected representative AE events (waveform, Fourier spectrum and spectrogram, from the top to the bottom of each section), event occurrence time is highlighted in (f) with the vertical black dashed lines. The differential stress is constant (75% of the residual value after failure) in both tests.

Figure 9 Cooling stages (from 65°C to 50°C) of G4 and G5 triaxial tests. (a) AE hits/minute and, sample temperatures and differential stress of G5 test (dry). From (b) to (e), selected representative AE events (waveform, Fourier spectrum and spectrogram, from the top to the bottom of each section), event occurrence time is highlighted in (a) with the vertical black dashed lines. (f) AE hits/minute and, sample temperatures and differential stress of G4 test (wet). From (g) to (l), selected representative AE events (waveform, Fourier spectrum and spectrogram, from the top to the bottom of each section), event occurrence time is highlighted in (f) with the vertical black dashed lines. The differential stress is constant (75% of the residual value after failure) in both tests.

Figure 10 AE-event location. (a-d) G5 dry sample, view of the 468 relocated events from the (a) north, (b) east, (c) south and (d) west face. (e-h) G4 wet sample, view of the 332 relocated events from the (e) north, (f) east, (g) south and (h) west face. Green and magenta diamonds refer to the

events occurred during the failure and heating stage of each test respectively. On each sample face, the macroscopic fracture traces are highlighted with the dashed lines.

Figure 11 AE parameters during the failure stages of G5 (left column) and G4 (right column) tests. (a, e) Maximum Amplitude; (b, f) maximum frequency peak; (c, g) kurtosis value; (d, h) duration. Gray and light blue diamonds refer to whole AE dataset (events with clear onset on at least 6 channels) and the localized AE events respectively.

Figure 12 AE parameters during the heating/cooling stages (from room temperature to 65°C/from 65°C to 60°C) of G5 (left column) and G4 (right column) tests. (a, e) Maximum Amplitude; (b, f) maximum frequency peak; (c, g) kurtosis value; (d, h) duration. Gray and light blue diamonds refer to whole AE dataset (events with clear onset on at least 6 channels) and the localized AE events respectively.

Table 1 30-minute time windows showing clusters of more than 5 MS events and related relationship with the rainfall amount and temperature variations in the half hour before and after the reported start time.